Observations of the Discrete Propagation of a Mesoscale Convective System during RELAMPAGO–CACTI

KELLY LOMBARDO[a] AND MATTHEW R. KUMJIAN[a]

[a] *Department of Meteorology and Atmospheric Science, The Pennsylvania State University, University Park, Pennsylvania*

(Manuscript received 1 October 2021, in final form 10 May 2022)

ABSTRACT: During the early morning hours of 5 November 2018, a mature mesoscale convective system (MCS) propagated discretely over the second-most populous province of Argentina, Córdoba Province, during the Remote Sensing of Electrification, Lightning, and Mesoscale/Microscale Processes with Adaptive Ground Observations–Cloud, Aerosol, and Complex Terrain Interactions (RELAMPAGO–CACTI) joint field campaigns. Storm behavior was modified by the Sierras de Córdoba, a north–south-oriented regional mountain chain located in the western side of the province. Here, we present observational evidence of the discrete propagation event and the impact of the mountains on the associated physical processes. As the mature MCS moved northeastward and approached the windward side of the mountains, isolated convective cells developed downstream in the mountain lee, 20–50 km ahead of the main convective line. Cells were initiated by an undular bore, which formed as the MCS cold pool moved over the mountain ridge and perturbed the leeside nocturnal, low-level stable layer. The field of isolated cells organized into a new MCS, which continued to move northeastward, while the parent storm decayed as it traversed the mountains. Only the southern portion of the storm propagated discretely, due to variability in mountain height along the chain. In the north, taller mountain peaks prevented the MCS cold pool from moving over the terrain and perturbing the stable layer. Consequently, no bore was generated, and no discrete propagation occurred in this region. To the south, the MCS cold pool was able to traverse the lower-relief mountains, and the discrete propagation was successful.

KEYWORDS: Atmosphere; Complex terrain; Convective storms; Mesoscale processes; Mesoscale systems

1. Introduction

a. Fortuitous opportunity

The Remote Sensing of Electrification, Lightning, and Mesoscale/Microscale Processes with Adaptive Ground Observations (RELAMPAGO; Nesbitt et al. 2021) and Cloud, Aerosol, and Complex Terrain Interactions (CACTI; Varble et al. 2021) projects were sister field programs funded by the National Science Foundation and Department of Energy, respectively. These programs targeted the influence of the Argentine terrain on organized deep convective storm development, severity, and evolution. The joint domains of the projects were south of the city of Córdoba, located in west-central Argentina in the lee of the Sierras de Córdoba mountain range, which comprises a series of north–south-oriented, parallel ridges (Fig. 1). Peak elevations of the Sierras Chicas, the eastern-most ridge, are >1000 m, whereas peaks of the Sierras Grandes to their west exceed 2500 m.

A combination of assets, including three X-band radars, two C-band radars, a vertically pointing lidar, radiosondes, mesonets, portable surface stations (pods), and hail pads were deployed during the 19 intensive observing periods (IOPs) from 1 November to 15 December 2018. Though not a formal RELAMPAGO–CACTI mission target, the discrete propagation of a mesoscale convective system (MCS) due to the interaction between the storm, the mountains, and a nocturnal stable boundary layer was serendipitously observed during the initial phases of asset deployment for IOP2. Here, we present evidence of the physical mechanisms contributing to this behavior, through temporally and spatially fine-scale remote sensing, surface, and radiosonde data.

b. Background and motivation

MCSs are sustained through the continued generation of new convective cells along a preferred flank of the storm complex, often through lifting by the storm outflow gust front (e.g., Newton and Fankhauser 1975). Radar depictions of MCSs reveal visually smooth translations across Earth's surface owing to this cold-pool-driven cell generation. Under certain conditions, however, new cells form downstream of the gust front at a distance larger than can be explained by cold pool lifting arguments (i.e., tens of kilometers ahead of the cold pool leading edge), though close enough to be considered a by-product of the moving storm. As a mature MCS moves toward these newly developed cells, the cells may intensify and organize into the leading edge of a new MCS, as the parent convective line decays (Houze 2004). The MCS appears to propagate discretely, or "jump forward," as observed through its radar reflectivity presentation. These are known as discrete propagation events.

MCSs have been observed to propagate discretely over inland regions and across coastlines, during day and night, emphasizing the ubiquity of the atmospheric conditions necessary to support such an evolution. Some of the earliest observations of discretely propagating MCSs were gathered during the Global Atmospheric Research Program (GARP) Atlantic Tropical Experiment (GATE) over tropical western Africa (Houze 1977; Fortune 1980). Isolated convective cells were observed to form "well ahead" of the parent squall line, hypothesized to form independently of the existing storm. These cells intensified and subsequently "merged" into the parent storm convective line, as the mature squall line neared. Based on early numerical

Corresponding author: Kelly Lombardo, lombardo@psu.edu

DOI: 10.1175/MWR-D-21-0265.1

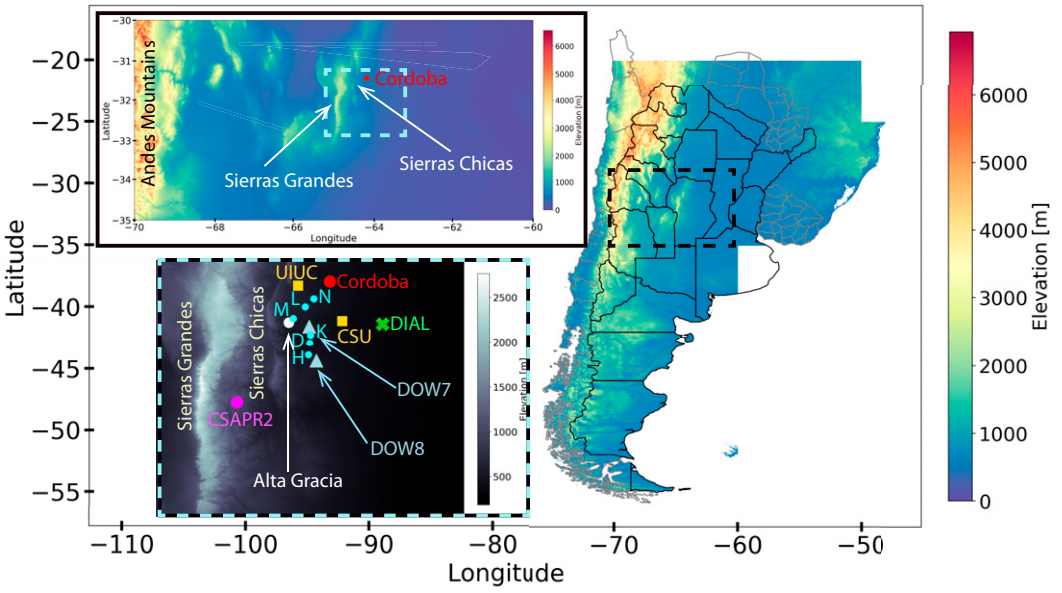

FIG. 1. Terrain map of Argentina, including a zoomed-in panel (top inset) illustrating the location of the mountain ranges (Andes Mountains; Sierras de Córdoba, which is composed of the Sierras Grandes and Sierras Chicas), and a zoomed-in panel (bottom inset) illustrating the location of the field assets on 5 Nov 2018. The city of Córdoba and its RMA1 radar are marked with a red circle, DOWs are marked with light blue triangles, the CSAPR2 is marked with a magenta circle, UIUC and CSU sounding mobile platforms are marked with golden squares (UIUC1 and UIUC2 are collocated), surface pods are marked with cyan circles (pod reference letters are included adjacent to the pod locations), the DIAL is marked with a green X, and the city of Alta Gracia is marked with a white circle.

modeling experiments, it was hypothesized that the convective cells initiated in response to upward motion caused by the formation of an adiabatically generated surface low, itself associated with compensating subsidence from the convective line (Rosenthal 1980). It was later hypothesized that convection initiated due to broad ascent ahead of the main convective line, which lifted air close to saturation, thus creating a more favorable environment for convection initiation (CI); however, the source of this ascent was not discussed (Crook and Moncrieff 1988). Compensating subsidence was instead shown to form in association with the new convective cells, which subsequently "propagated away in the form of a deep gravity wave" (Crook and Moncrieff 1988).

Later theoretical studies of tropical MCSs attributed the development of the downstream ascent to low-frequency gravity waves, referred to as "buoyancy bores" by the author owing to the net vertical displacement of the tropospheric layer (Mapes 1993). The low-frequency waves were generated by latent heating and cooling associated with an MCS. As these waves propagated ahead of the storm, the ascent associated with the different wave modes caused an upward displacement and cooling of the downstream environment. Cooling was maximized in the midlevels, which decreased the stability of the lower troposphere, created a more favorable environment for CI, and promoted the eventual discrete propagation of the MCS. Follow-up studies emphasized the role of such low-frequency gravity waves in modifying the environment in support of CI and cell growth (Lane and Reeder 2001; Fovell 2002; Fovell et al. 2006; Bryan and Parker 2010; Su and Zhai 2017; Adams-Selin 2020). Several have shown that lower-tropospheric lifting by low-frequency "$n = 1$" (Su and Zhai 2017) and "$n = 2$" (Lane and Reeder 2001; Fovell et al. 2006; Bryan and Parker 2010; Adams-Selin 2020) wave modes can temporarily decrease the ambient static stability or increase the surface-based convective available potential energy (SBCAPE) on the order of 200 J kg^{-1}.

While low-frequency waves can create a more favorable environment for CI, cell initiation requires ascent from a more localized source, such as high-frequency gravity waves. Fovell et al. (2006) illustrated the importance of high-frequency gravity waves, generated through "fluctuations" in latent heating/cooling associated with MCS cell regeneration, in CI ahead of the primary MCS and its discrete propagation. High-frequency gravity waves were shown to be important for downstream CI and MCS discrete propagation in coastal regions as well. Lombardo (2020) attributed the discrete propagation of a coastal MCS to the interaction between storm-generated high-frequency gravity waves and those generated by the sea breeze front. The constructive interference of these waves generated deep ascent downstream of the storm, and initiated convection. In contrast, Lombardo and Kading (2018) found a reduction of the LFC in the storm-modified environment allowed sea breezes in close proximity to initiate deep convective cells contributing to coastal MCS discrete propagation.

Others have highlighted the importance of atmospheric bores in the discrete propagation of MCSs, whose cold pools often initiate the bore responsible for the downstream CI (Haghi et al. 2017; Johnson et al. 2018). For example,

maintenance of the 15 July 2015 nocturnal MCS observed during Plains Elevated Convection At Night (PECAN; Geerts et al. 2017) was due to the generation of cells along and behind a bore located tens of kilometers downstream of the MCS (Grasmick et al. 2018). Further, through an evaluation of 13 bores observed during the International H_2O Project (IHOP) over the southern Great Plains, Parsons et al. (2019) found bores to be important for CI, but also for the reduction of CIN in their wake, consistent with other case study analyses (Koch et al. 2008b; Zhang et al. 2020).

Much of what we know about the discrete propagation of MCSs—particularly the underlying physical processes—was learned from theory, numerical modeling, and a limited number of observed events. The temporal and spatial frequency of observations necessary to further our understanding of discrete propagation processes are only acquired during field campaigns, such as IHOP and PECAN. The observations gathered of a discrete propagation event during RELAMPAGO–CACTI offer a somewhat rare opportunity to advance our understanding, evaluate the validity of the processes gleaned from theory and numerical models, and add to the small body of literature documenting these events. Additionally, to our knowledge, this is the first observational analysis performed of a discrete propagation event near substantial topographic relief, which we show dramatically impacts storm behavior. The presentation of this case is as follows. Section 2 details the deployed instrumentation. An event overview through stationary radar platforms is provided in section 3, followed by a discussion of the evolving environment in section 4. The physical mechanism driving the discrete propagation is presented in sections 5, and its role in CI is discussed in section 6. An evaluation of the ability of the environment to support bores and gravity waves is presented in section 7. The impact of the Sierras de Córdoba is discussed in section 8. A summary is provided in section 9.

2. Data

The discrete propagation of the Argentine MCS occurs during the early morning hours of 5 November 2018, between 0800 and 1000 UTC, corresponding to 0500–0700 local time (LT). Sunrise occurs at 0617 LT on this day. The event is observed by two C-band and two X-band radars, a vertically pointing lidar, surface pods, and radiosondes (Fig. 1). The MCS approaches the network of instruments from the southwest, moving over the majority of the assets, providing a unique and invaluable dataset documenting the discrete propagation of the system, including the impact of the regional mountains. A list of deployed assets and their surface elevations is provided in Table 1.

a. *Remote sensing observations*

The northern edge of the MCS passes <30 km to the south of the RMA1 C-band (5.4-cm wavelength), dual-polarization Doppler weather radar, permanently located in the city of Córdoba, Argentina (Fig. 1, red circle) at 395 m above mean sea level (MSL; Table 1). The RMA1 is operated by the National System of Meteorological Radars (SINARAME; in Spanish) for the Servico Meteorólogico Nacional (SMN) of Argentina. Plan position indicator (PPI) scan data from 0.5° elevation angle are available at ~9-min intervals. The Department of Energy (DOE) second generation Doppler polarimetric C-Band Scanning Atmospheric Radiation Measurement (ARM) Precipitation Radar (CSAPR2) facility is temporarily stationed ~90 km south-southwest of Córdoba during CACTI. The radar is located within the Sierras de Córdoba at 1131 m MSL (Fig. 1, magenta circle; Table 1). Data from both 0.5° elevation angle PPI and multiple hemispheric range–height indicator (RHI) scans are available as the MCS moves over the radar site during its discrete propagation (for details on the scanning strategies employed, see Varble et al. 2021).

TABLE 1. Surface elevation (above sea level) of deployed assets.

Assets	Elev (m)
Radars	
RMA1	438
DOW7	518
DOW8	482
CSAPR2	1142
Lidars	
DIAL	333
Soundings	
UIUC2 0807 UTC	586.8
COR 0819 UTC	490
UIUC1 0832 UTC	592.8
UIUC2 0903 UTC	586.8
CSU 0858 UTC	391.5
CSU 1000 UTC	391.5
CSU 1100 UTC	389.5
Pods	
H	512.8
D	475.1
K	492.1
M	563.7
L	466.7
N	530.8

Two mobile X-band (~3.2-cm wavelength) Doppler on Wheels (DOW; Wurman et al. 2012) radars owned and operated[1] by the Center for Severe Weather Research (CSWR) during this event are positioned between the C-band radars in the lee of the Sierras de Córdoba (Fig. 1, light blue triangles). Their fortuitous positions for the upcoming IOP later that morning provide an opportunity for close-proximity observations as the MCS approaches, passes over, and moves away from the DOWs. During the event, the scanning strategy includes PPI scans at 22 elevation angles between 0.5° and 50°. To the east of the DOWs, the National Center for Atmospheric Research (NCAR) vertically pointing water vapor micropulse differential absorption lidar (DIAL) is located 40 km southeast of Córdoba, near the city of Pilar (Fig. 1, green X marker). The DIAL operates at 828.2-nm wavelength, with a vertical range of 300–4000 m and 150-m vertical resolution.

[1] The DOWs are currently affiliated with the University of Illinois at Urbana–Champaign.

Data are processed at a 37.5-m spatial base resolution and 1-min temporal resolution. Data are then smoothed spatially and temporally using a Gaussian kernel, optimized to minimize errors due to random noise and smearing. Regions of high backscatter gradients (i.e., near clouds) are poorly resolved and therefore masked due to the known biases in water vapor estimates. A Gaussian smoothing kernel of 125 m and 5 min is then applied to the masked fields to develop the final product.

b. *Thermodynamic and kinematic observations*

Mobile radiosonde sounding unit site positions and release times are based on the needs of the formal RELAMPAGO IOP later that morning, though their locations and initial releases observe the evolving environment associated with the discretely propagating MCS. Two mobile GRAWMET 5.14 radiosonde systems with GRAW DFM-09 radiosondes, operated by the University of Illinois at Urbana–Champaign (UIUC1 and UIUC2), are collocated 20 km west-southwest of Córdoba (Fig. 1, gold square). One mobile MW41 2.2.1DigiCORA radiosonde system with Vaisala RS41-SG radiosondes, operated by Colorado State University (CSU), is located 30 km southeast of Córdoba (Fig. 1, gold square). Quality controlled, 5-m vertical resolution multi-network composite highest resolution radiosonde data from these mobile units are available from the University Corporation for Atmospheric Research (UCAR)/NCAR Earth Observing Laboratory (EOL; UCAR/NCAR Earth Observing Laboratory 2020). We perform additional quality-control measures (see the appendix) to remove near-surface biases from several of these soundings. Complementary to the mobile units, the SMN operates six Modem GPSsonde M10 radiosonde systems at permanent locations within central Argentina, including Córdoba, during RELAMPAGO (Servicio Meteorólogico Nacional, Argentina 2019).

CSWR also deploys mobile 1-m surface weather stations, known as pods, along a north–south-oriented line extending 50 km south of Córdoba (Fig. 1, cyan circles). Pods observe temperature, relative humidity, pressure, wind speed, and wind direction (blade and sonic anemometers) at 1-Hz intervals. All data are quality controlled to correct for heading and anemometer orientation issues.

3. The 5 November 2018 discrete propagation event

a. *Overview as observed by stationary radar platforms*

At the event onset, convection initiates southwest of the Sierras de Córdoba and organizes into a MCS during the overnight hours of 5 November 2018 (not shown). The northwest–southeast-oriented MCS moves northeastward and approaches the Sierras de Córdoba from the southwest, as depicted in the RMA1 radar reflectivity factor at horizontal polarization (Z_H) PPI scans (Figs. 2a–e). Near 0854 UTC (0554 LT), the MCS begins to weaken (Fig. 2f), as individual convective cells form 20–50 km to its northeast along a line parallel to the primary storm. Over the following 20 min, the intensity, number, and coverage of the new cells increase (Fig. 2g). These cells organize into the leading line of a new MCS as the parent storm decays (Fig. 2h). The apparent jump in the location of the MCS main convective line marks the discrete propagation.

CSAPR2, the southern-most radar platform, offers complementary evidence of the discrete propagation from an independent source and location. Its scanning strategy includes alternating, interspersed RHI scans, which offer a unique perspective of the downstream cell initiation and eventual storm redevelopment. At approximately 0815 UTC (0515 LT), the initial MCS moves northeastward over the CSAPR2 prior to its discrete propagation (Figs. 3a and 4a). As the storm moves away from the radar, isolated cells form 20–30 km ahead of the primary storm, visible in both the PPI and RHI Z_H scans (Figs. 3b and 4b). Within 15 min, cell number and coverage increase (Figs. 3c and 4c). By 0912 UTC (0612 LT), the cells deepen and their Z_H increases indicating their intensification as they approach the edge of the CSAPR2 radar domain (Figs. 3d and 4d).

b. *CI relative to a moving convergence boundary*

Convection initiation associated with the discrete propagation occurs behind a northeastward-moving boundary (i.e., a line of convergence) visible in DOW7 low-level radial velocity (v_r) scans (Fig. 5, annotated with a black dashed line) located ahead of the enhanced outbound ($v_r > 0$ m s^{-1}) values north-northeast of the radar. At 0834 UTC, the northwest–southeast-oriented convergence line is located 10 km northeast of DOW7 (Fig. 5a). Beam blockage to the southeast of DOW7 prevents a view of the boundary in this location, and the later initial scanning time of DOW8 (scans begin at 0900 UTC) prevents the analysis of DOW8 data at this point in the evolution. At this time, the MCS is located upstream of the Sierras Chicas, as evident in the 5.5° PPI Z_H data from DOW7 (Fig. 6a). The higher elevation-angle scan for the Z_H data provides a view of the convective evolution, while limiting ground clutter and beam-blockage by the terrain to the southeast of DOW7.

Over the following 30 min, the MCS attempts to cross the mountains from southwest to northeast (Figs. 6b–d). Meanwhile, the boundary moves northeastward at ~16.5 m s^{-1} away from the terrain (Figs. 5b–d). Isolated cells form in the Argentine plains behind the boundary (Figs. 6b–d). CI primarily occurs behind the southern portion of the boundary, while few cells initiate behind the northern portion. We hypothesize that the mountains play a role in limiting CI and the discrete propagation of the northern segment of the MCS, which will be addressed in section 7. The southern segment of the MCS redevelops and moves to the northeast, while the convergence boundary remains ahead of the new convection (Figs. 5e,f and 6e,f). The northern portion of the parent MCS stalls over the mountains with no downstream development. After 0920 UTC, it becomes challenging to identify the location of the convergence boundary, either due to its weakening or as a consequence of its greater distance from the radar (Fig. 5f). Cells grow upscale into an MCS and move out of radar range (Figs. 6g–j), as also observed by RMA1 and CSAPR2.

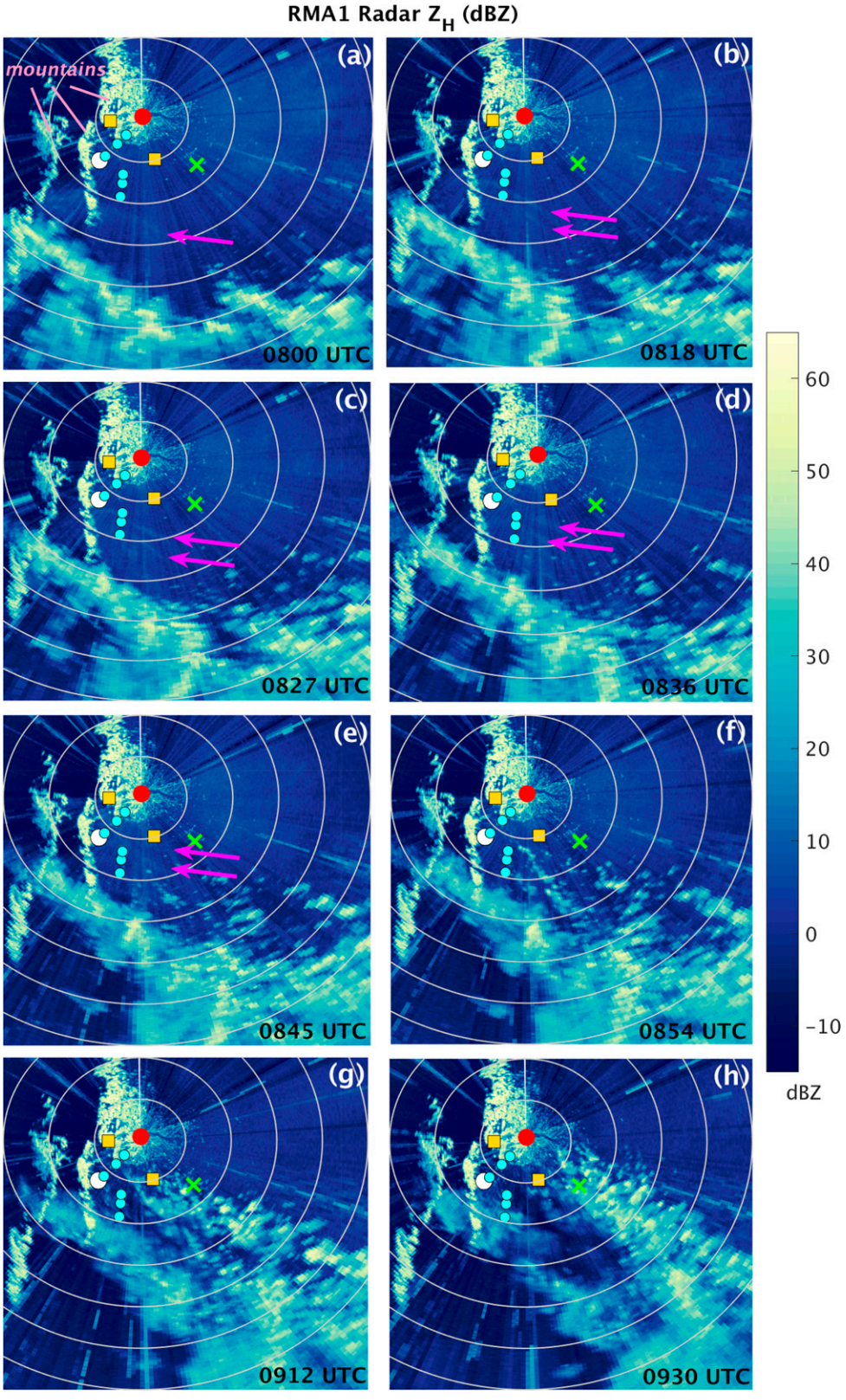

FIG. 2. Córdoba RMA1 0.55° PPI reflectivity factor at horizontal polarization (Z_H; dBZ according to outset scale) at (a) 0800, (b) 0818, (c) 0827, (d) 0836, (e) 0845, (f) 0854, (g) 0912, and (h) 0930 UTC 5 Nov 2018. Markers are as in Fig. 1. Range rings are marked in 25-km intervals. Magenta arrows identify the fine lines associated with an undular bore.

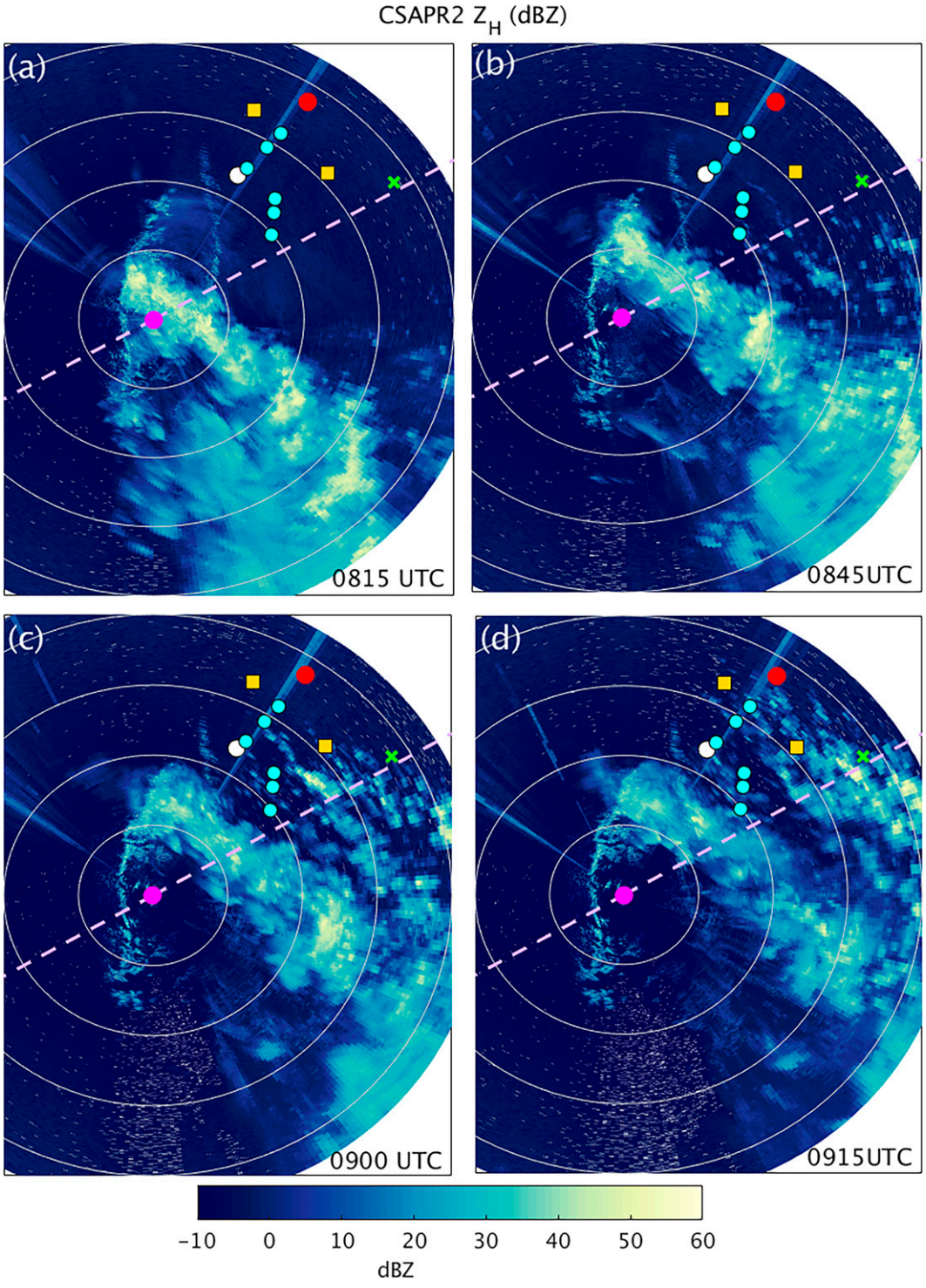

FIG. 3. CSAPR2 0.5° PPI of Z_H at (a) 0815, (b) 0845, (c) 0900, and (d) 0915 UTC 5 Nov 2018. Range rings are marked in 25-km intervals. Colored markers are as in Fig. 1. The lavender dashed line shows the 60° azimuth along which the hemispheric RHI scan shown in Fig. 4 is taken.

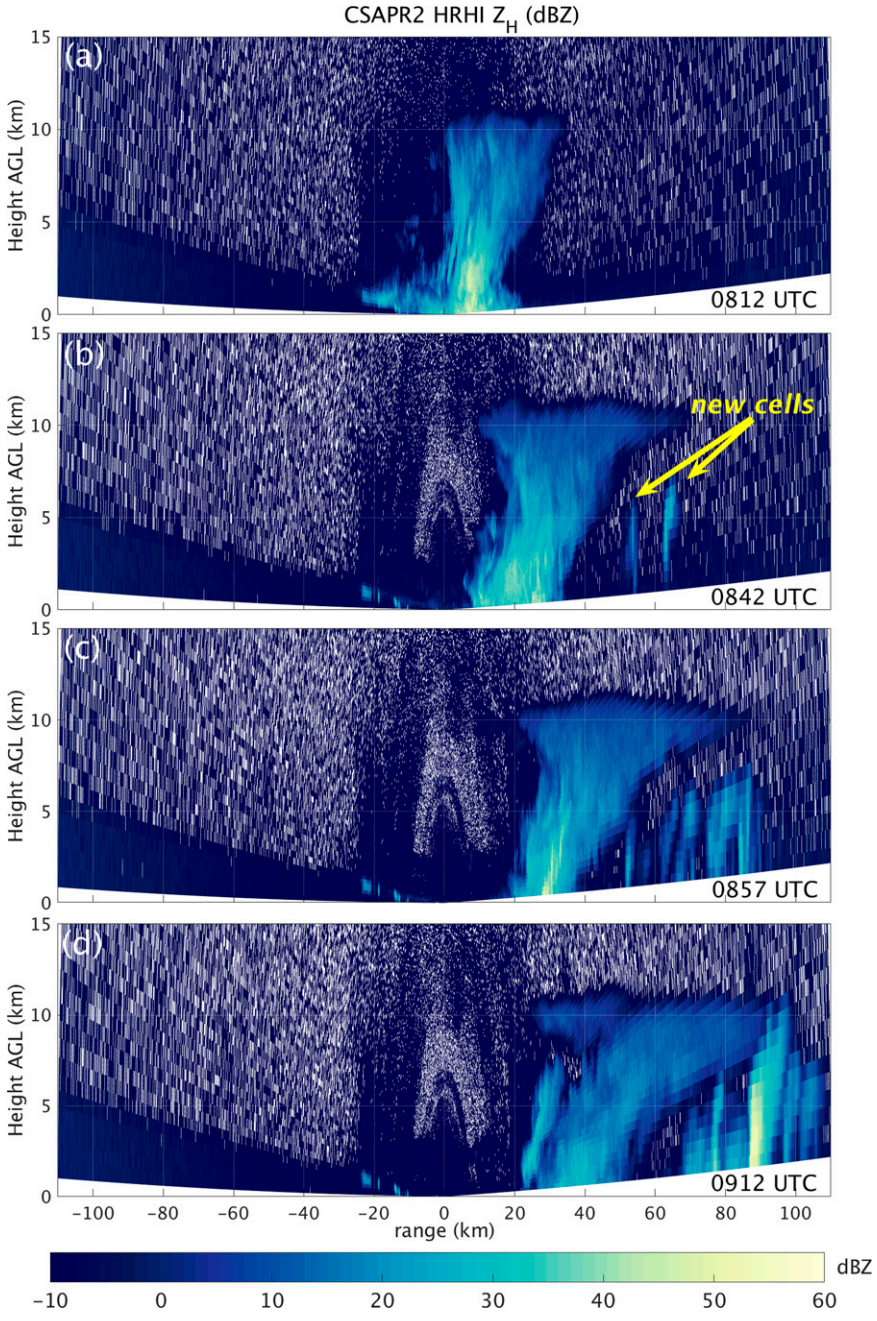

FIG. 4. CSAPR2 60° azimuth hemispheric RHI of Z_H (dBZ) at (a) 0812, (b) 0842, (c) 0900, and (d) 0912 UTC 5 Nov 2018. Yellow arrows indicate the new cells that become the new MCS leading convective line. Note the difference in scales between the ordinate and abscissa.

4. Evolution of the environment

Exploration of the evolving environment provides insight into the location of CI with respect to the moving convergence boundary (i.e., behind the boundary), and context for a deeper understanding of the nature of the moving boundary. The initial sounding of the IOP is released from the UIUC2 mobile unit (Fig. 7a) and illustrates the undisturbed ambient environment northeast of the boundary (Figs. 1 and 2a).[2] At 0807 UTC (0507 LT), a weak low-level nocturnal inversion, with a top located near 880 hPa (~540 m above ground level, AGL), resides over an isothermal surface-based layer. The

[2] Profiles may be influenced by the Sierras Chicas given their launch point location in the mountain lee.

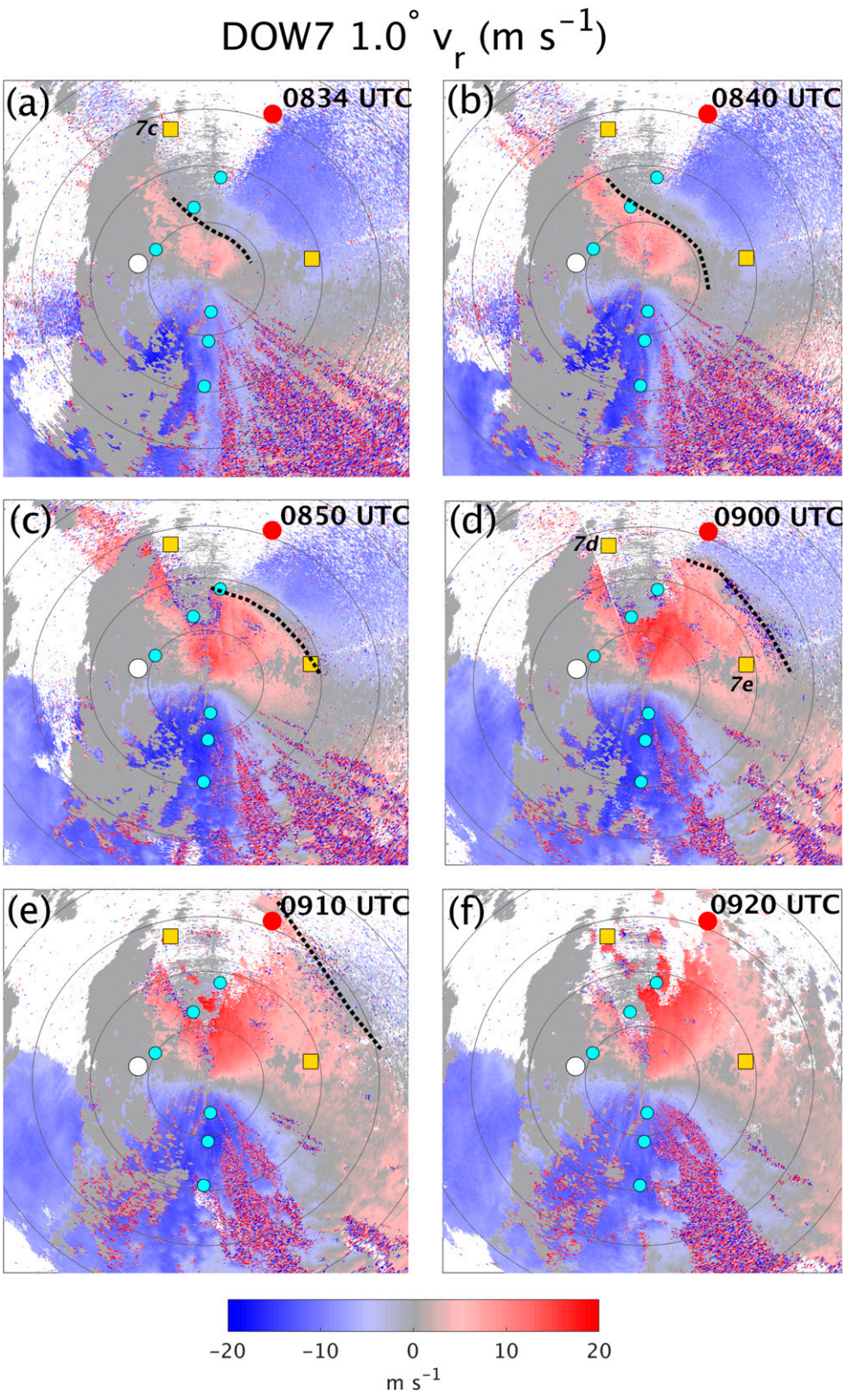

FIG. 5. DOW7 1.0° PPI of radial velocity (v_r; m s^{-1} according to outset scale) at (a) 0834, (b) 0840, (c) 0850, (d) 0900, (e) 0910, and (f) 0920 UTC 5 Nov 2018. Range rings are marked in 10-km intervals. Colored markers are as in previous figures. Black dashed lines identify the approximate leading edge of the northeastward-moving boundary. Numbers next to sounding locations correspond to soundings shown in Fig. 7. The Sierras Chicas are visible as gray shading to the west of DOW7.

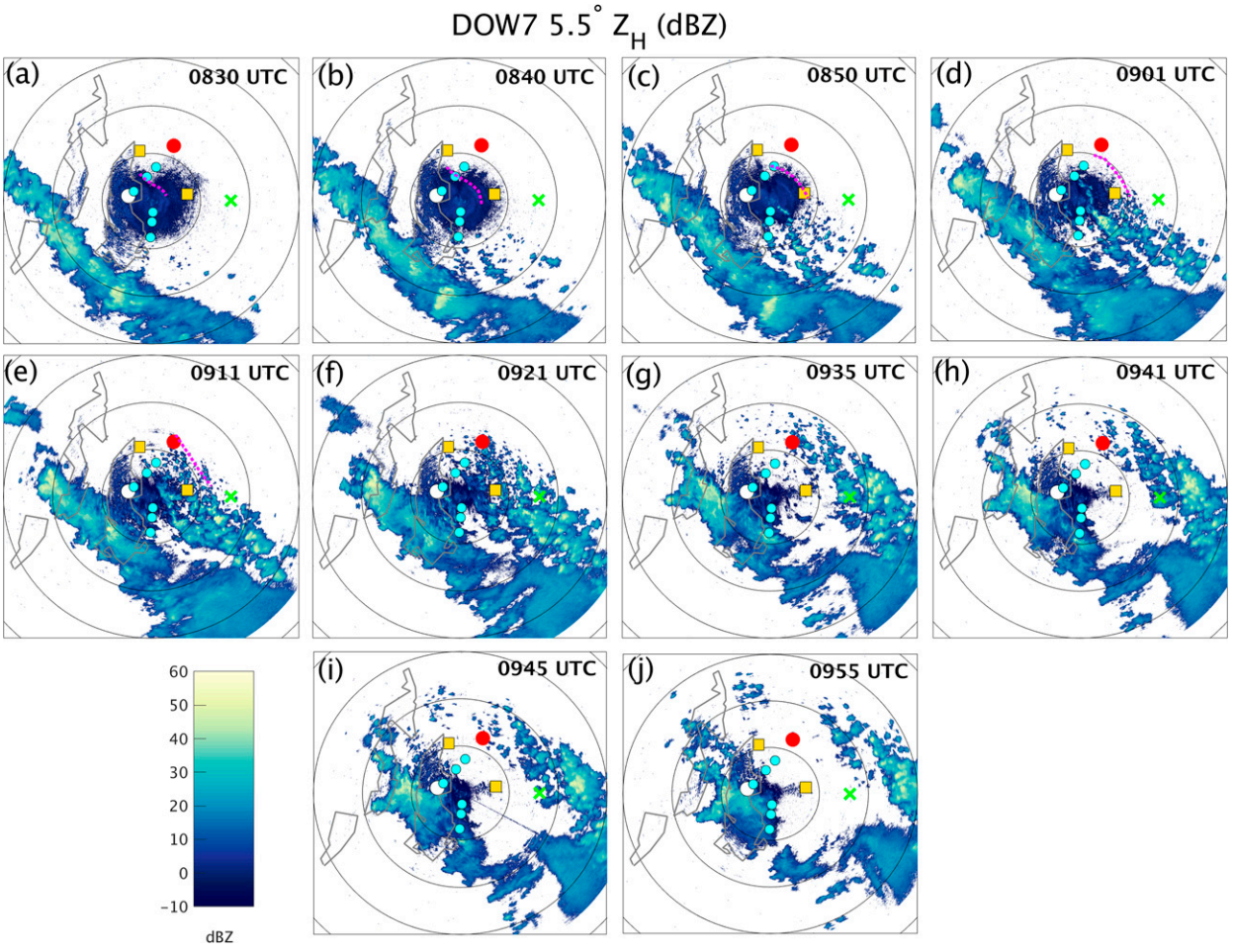

FIG. 6. DOW7 5.5° PPI of Z_H at (a) 0830, (b) 0840, (c) 0850, (d) 0901, (e) 0911, (f) 0921, (g) 0935, (h) 0941, (i) 0945, and (j) 0955 UTC 5 Nov 2018. Range rings are marked in 25-km intervals. Colored markers are as in previous figures. Magenta lines show the approximate leading edge of the northeastward-moving boundary identified in the previous figure. The approximate location of terrain is outlined in dark gray. Note, range rings are larger than in Fig. 5, and thus the Sierras Chicas and the eastern edge of the Sierras Grandes are visible.

top of a second, more stable inversion is located at 715 hPa (~2460 m AGL). This elevated mixed layer is likely advected east-southeastward by the midlevel flow, visible in the wind profile data, from its elevated origin over the 2000-m-tall peaks of the Sierras de Córdoba to over the Argentine Plain, as in the central United States (e.g., Banacos and Ekster 2010). The combination of warming through the bottom of the elevated mixed layer from warm-air advection between 750 and 700 hPa in conjunction with nocturnal radiative cooling below the layer helps to strengthen the capping inversion. A similar process may be occurring for the near-surface inversion as well, with relatively weaker warm-air advection between 875 and 825 hPa overlying the radiatively cooled air below. Though SBCAPE is limited (83 J kg^{-1}) and surface-based CIN (SBCIN) is large (549 J kg^{-1}), there is instability available for elevated parcels (most-unstable CAPE of 1102 J kg^{-1}; Table 2). CAPE values reported may be underestimated since the balloon burst before reaching the tropopause, though the 430-hPa surface-based equilibrium level suggests that measurements of the tropospheric instability were likely complete prior to the balloon bursting (Fig. 7a).

Over the following 25 min, the local environment remains relatively homogeneous in space and time (Figs. 7b,c). Similar conditions are apparent in the Córdoba sounding released 15 km east of and 12 min after the UIUC2 sounding (Fig. 7b). SBCAPE is ~100 J kg^{-1} larger and most-unstable CAPE (MUCAPE) is ~400 J kg^{-1} larger (Table 2), which may be a consequence of the slightly steeper lapse rates above 500 hPa, highlighted by an evaluation of the temperature difference through the profile (Fig. 8, navy line). Over Córdoba, temperatures are 1°–2°C greater between 6000 and 7000 m (450–430 hPa) and near 1°C smaller between 7000 and 9000 m (429–307 hPa) as compared to UIUC2 0807 UTC, leading to steeper lapse rates and a higher equilibrium level located near 300 hPa. At 0832 UTC, a similar warming is observed at the UIUC1 launch point (Fig. 7c; Fig. 8, blue line) supporting 242 J kg^{-1} larger MUCAPE, as compared to UIUC2 at 0807 UTC (Table 2). Temperature changes near 2750 m (730 hPa) at both COR and

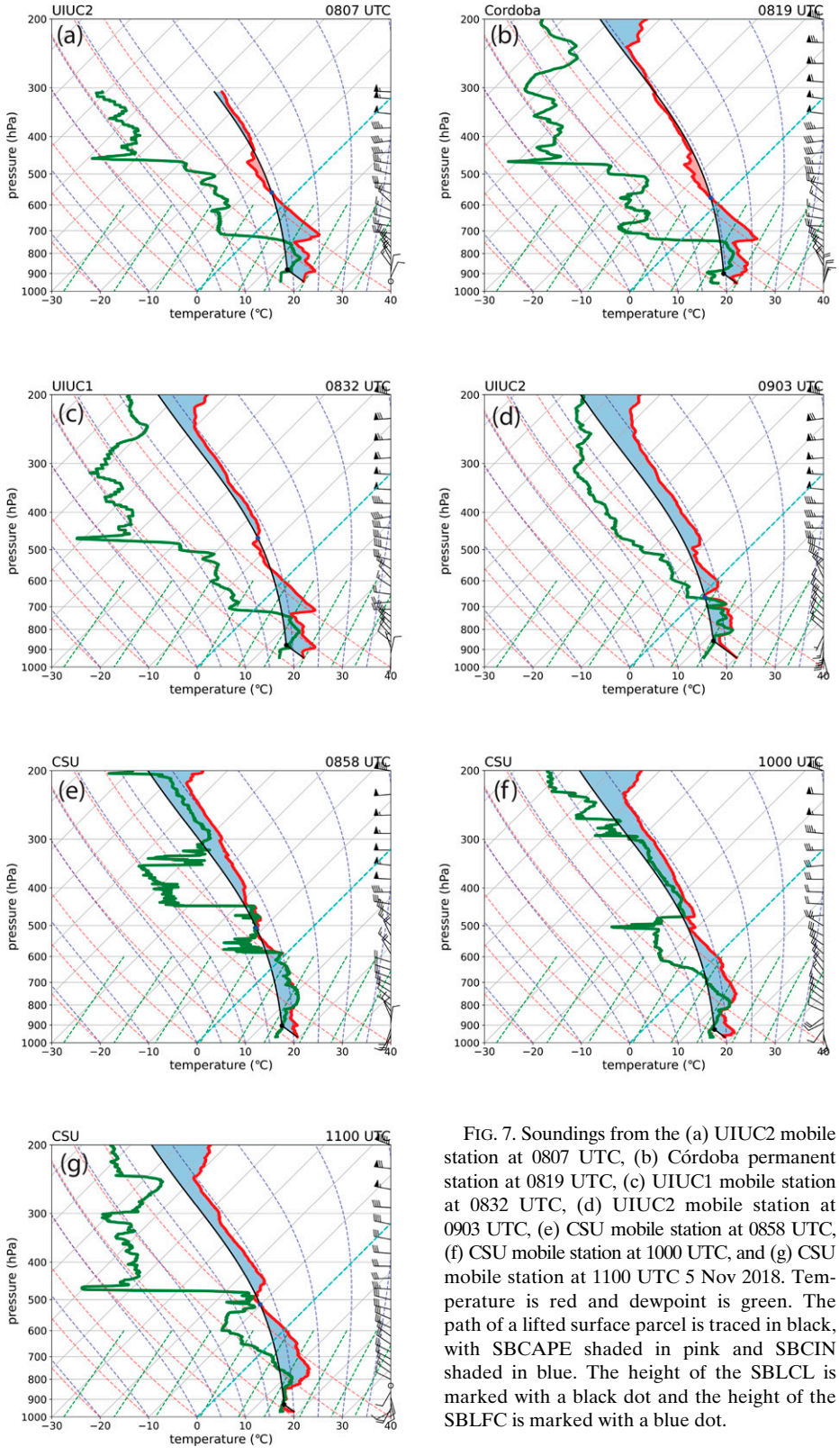

FIG. 7. Soundings from the (a) UIUC2 mobile station at 0807 UTC, (b) Córdoba permanent station at 0819 UTC, (c) UIUC1 mobile station at 0832 UTC, (d) UIUC2 mobile station at 0903 UTC, (e) CSU mobile station at 0858 UTC, (f) CSU mobile station at 1000 UTC, and (g) CSU mobile station at 1100 UTC 5 Nov 2018. Temperature is red and dewpoint is green. The path of a lifted surface parcel is traced in black, with SBCAPE shaded in pink and SBCIN shaded in blue. The height of the SBLCL is marked with a black dot and the height of the SBLFC is marked with a blue dot.

TABLE 2. Sounding parameters. MUParcel = most-unstable parcel.

	UIUC2 0807 UTC	COR 0819 UTC	UIUC1 0832 UTC	CSU 0858 UTC	UIUC2 0903 UTC
SBCAPE (J kg^{-1})	83	181	39	6	0
MUCAPE (J kg^{-1})	1102	1521	1344	6	1383
SBCIN (J kg^{-1})	549	520	509	422	261
MUCIN (J kg^{-1})	8	20	6	422	0
MUParcel (hPa)	822.1	858.1	815.5	754.7	802.5
MUParcel (m MSL)	1770	1390	1855	2483	1980
SBLCL (hPa)	880.1	900.6	887.5	903.3	855.4
SBLCL (m MSL)	1185	973	1125	968	1440
SBLFC (hPa)	557.6	574.9	466.6	506.5	661.9
SBLFC (m MSL)	4965	4721	6340	5684	3580
0–1-km shear (m s^{-1})	6.2	6.6	7.7	7.8	12.9
0–6-km shear (m s^{-1})	19.1	20.8	20.5	18.5	24.6

UIUC1 are associated with subtle differences in the altitude of the midlevel inversion (Fig. 8). All three soundings sample the atmosphere northeast of the convergence boundary, prior to its passage (Fig. 5a).

The next series of radiosondes are released after the boundary passes over their launch locations (Figs. 5d,e) and notable differences develop within the lower troposphere. The UIUC2 sounding released at 0903 UTC (0603 LT) shows a shift to strong southerly winds (15 m s^{-1}) within the lowest 1.8 km, with clockwise turning winds through the layer (Fig. 7d). Heights of both the near-surface and elevated inversions increase, and the inversion layers cool and moisten. The height of the near-surface inversion nearly doubles, rising 848 m, while the air temperature at the apex of the inversion decreases 7.7°C. This increase in inversion height and cooling through the layer suggest ascent either has occurred or is occurring. Below the inversion, temperatures decrease as much as 4°–5°C (Fig. 8, cyan line) due to the vertical displacement of the warm nose and cooling associated with ascent. The top of the elevated inversion increases 1078 m and the air at the apex cools 11°C. Temperatures decrease more than 6°C underneath the inversion, again associated with lifting of the inversion layer (Fig. 8, cyan line). Consequently, SBCIN is reduced from ~500 to ~260 J kg^{-1} (Table 2) and MUCIN becomes zero, which is a more favorable environment for CI and consistent with cells forming behind the moving boundary.

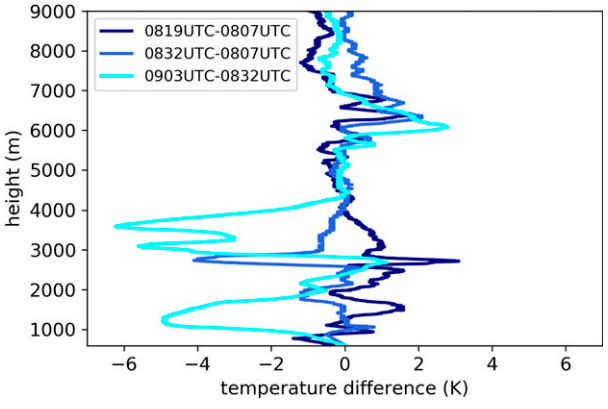

FIG. 8. Vertical profile (m MSL) of the difference in temperature (K) for the Cordoba 0819 UTC minus UIUC2 0807 UTC (navy), UIUC1 0832 UTC minus UIUC2 0807 UTC (blue), and UIUC2 0903 UTC minus UIUC1 0832 UTC (cyan) soundings.

The CSU mobile team, located 35 km to the southwest of UIUC2 (Fig. 1), releases a radiosonde simultaneously with the UIUC2 mobile team (Fig. 7e). A line connecting the UIUC2 location to the CSU location has an orientation parallel to the MCS. Thus, an evaluation of the 0858 UTC CSU sounding data, in the context of the UIUC2 0903 UTC data, highlights the heterogeneity of the environment behind the boundary and ahead of the parent MCS. One important similarity of the CSU and UIUC2 environments is the presence of strong southerly winds within the lowest 500 m, which indicates that the boundary moved past the CSU location at this time; however, the more northern location of the UIUC2 sounding places it within the area where CI is limited, while the southern CSU sounding is released among the developing cells and thus is convectively contaminated (Fig. 6d). Due to the ongoing convection, CSU MUCAPE is near zero, with SBCIN > 400 J kg^{-1} (Table 2).

Then, 30 min later (0935 UTC; not shown), sounding data from UIUC1 illustrate that the near-surface inversion height remains elevated, and strong southerly winds persist through the lower troposphere. This semipermanent change in lower-troposphere characteristics is important for the classification of the boundary, which is discussed in the following section.

5. Origin and nature of the moving boundary

The boundary's origin can be traced back to the parent MCS, and its propagation is visible in the Córdoba RMA1 radar Z_H PPIs (Fig. 2, highlighted by magenta arrows). Figure 9 shows the same data, but zoomed in (and with a reduced range of the Z_H color scale) to highlight the northeastward-moving fine lines associated with the boundary. The leading boundary is first visible at 0751 UTC (not shown), and by 0800 UTC, it is located ~30–40 km northeast of the MCS (Figs. 2a and 9a). Based on tracking the boundary in consecutive PPI scans, we estimate the feature moves northeastward at ~13–16.5 m s^{-1} (Figs. 2b–d and 9b–d); a similar estimate is

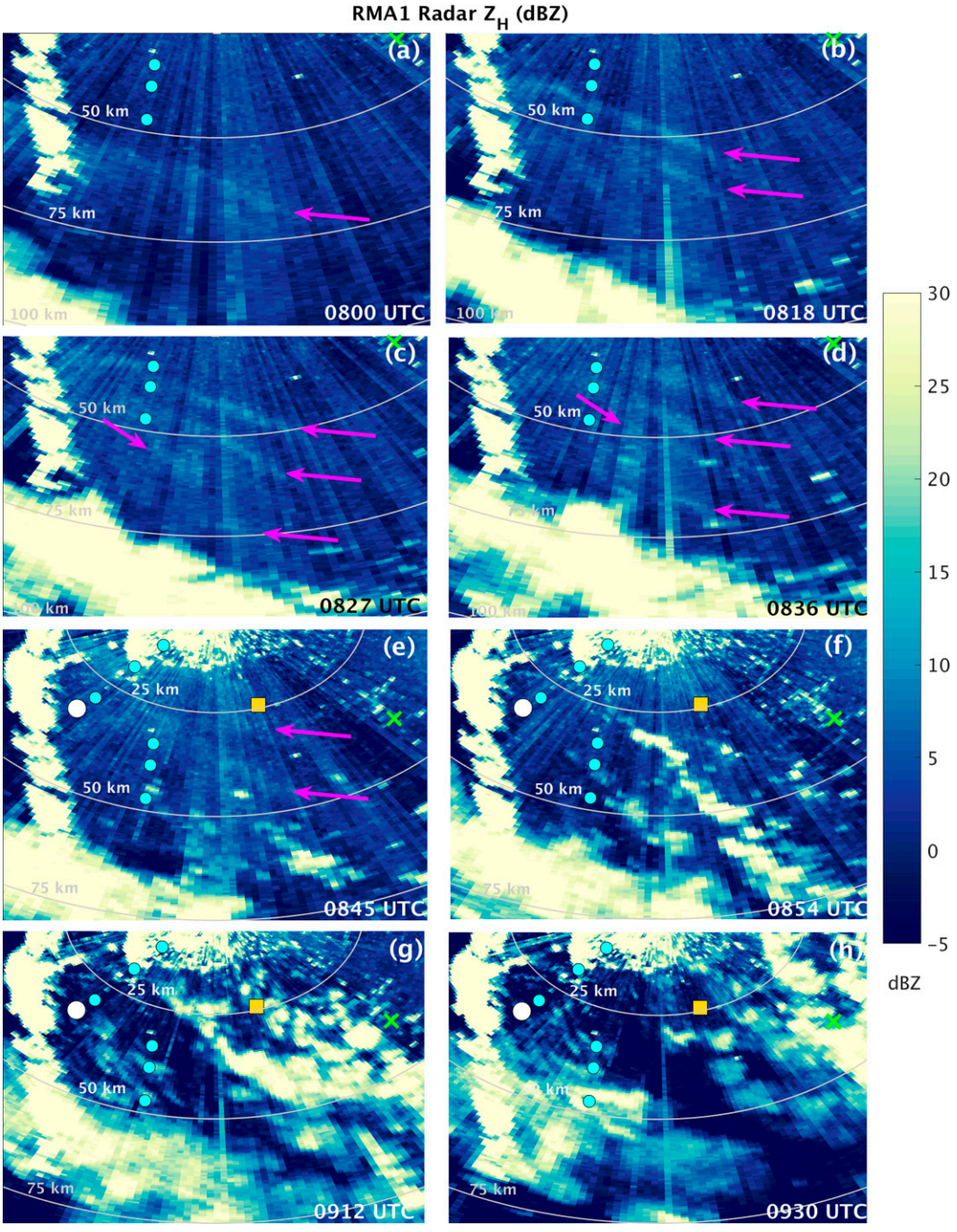

FIG. 9. As in Fig. 2, but zoomed in and with reduced Z_H range shown on the color scale to highlight the fine lines.

obtained using DOW7 data. By 0836 UTC, cells develop behind the boundary, as seen in the 0.5° Z_H scan (Figs. 2d and 9d). Precipitation from the initiating cells continues to be detected behind the boundary as it propagates northeastward (Figs. 2e–h and 9e,f). We hypothesize that the moving boundary is an undular bore (a bore with trailing gravity waves behind the bore front), generated though the interaction between the parent MCS cold pool and the early morning cool boundary layer confined in the mountain lee (Figs. 7a–c; e.g., Tepper 1950). Note that as many as four Z_H "fine lines" are evident in the RMA1 PPIs (Figs. 2 and 9), consistent with the identification of bores in prior studies (Haghi et al. 2017; Grasmick et al. 2018). The fine lines arise from lofting of biota or other small particles associated with convergence and ascent (e.g., Wilson and Schreiber 1986)—multiple lines as observed here implies the presence of an undular bore or soliton, a family of solitary

waves (Christie et al. 1978; Christie 1989; Fulton et al. 1990; Knupp 2006; Koch et al. 2008a,b; Grasmick et al. 2018). We manually estimated the spacing of these fine lines, which is a proxy for the wavelength, to be 8.2 ± 1 km. Similar wavelengths (~8 km) were observed with the NCAR S-band dual-polarization Doppler radar (S-Pol) for nocturnal solitary waves associated with bores that developed during IHOP (Weckwerth et al. 2004; Knupp 2006; Koch et al. 2008b).

The theoretical nature of bores, or bore type, is often determined by calculating the ratio between the mean depth of a bore moving through a stable layer (h_1) and the initial depth of the undisturbed stable layer (h_0; Wood and Simpson 1984; Rottman and Simpson 1989). Smooth undular bores with multiple undulations behind the bore head (i.e., trailing gravity waves) and little mixing across the interface between the stable layer and overlying atmosphere (type A) are observed when $1 < h_1/h_0 < 2$. For $2 < h_1/h_0 < 4$, undular bores are observed with mixing across the stable layer interface (type B) due to shearing instabilities. For $h_1/h_0 > 4$, mixing dominates the motion on the rearward side of the bore head, which removes the additional trailing undulations and has the potential to mix elevated air down to the surface. Given that radar observations suggest the presence of an undular bore, we evaluate this theoretical relationship in support of this assertion. We hypothesize that there exist two levels within the atmosphere capable of supporting bores, particularly the near-surface and elevated inversions; an analysis is performed and presented in section 7 to support our hypothesis that the environment is capable of supporting bores within two levels. Thus, the theoretically predicted bore type is evaluated for both levels. Calculations are performed using the UIUC2 0807 UTC (pre-bore environment) sounding for the two observed stable layers. For the near surface inversion, $h_1/h_0 = 2.57$ indicates an undular bore with mixing along the interface in this lower level. For the elevated inversion, $h_1/h_0 = 1.44$ indicates a smooth undular bore with little to no mixing. Thus, the fine lines observed on radar are consistent with an undular bore.

Calculations of the theoretical speeds of a bore moving through these two inversion layers align with observation-based estimates. Theoretical bore speed calculations are performed using the 0807 UTC (pre-bore environment) and 0903 UTC (post-bore environment) soundings launched by the UIUC2 group, to retain consistency in launch team and surface elevation between the two vertical profiles (e.g., Fig. 7a). Based on Coleman et al. (2010), the theoretical speed of a bore can be calculated as

$$c_{\text{bore}} = \left[g \frac{\Delta\theta_v}{\theta_v} \frac{h_1}{2} \left(1 + \frac{h_1}{h_0} \right) \right]^{1/2}, \tag{1}$$

where θ_v is the average virtual potential temperature in the stable layer, $\Delta\theta_v$ is the difference between the average θ_v in the stable layer and that in the less stable layer above, h_0 is the initial depth of the stable layer, and h_1 is its average post-bore depth. Based on vertical profiles of temperature (Fig. 7a) and θ_v (Fig. 10a), the height of the near surface inversion in the pre-bore environment is h_0 = 540 m AGL (1127 m MSL) and the height of the inversion following bore passage is h_1 = 1338 m AGL (1975 m MSL). The average θ_v through the stable layer is 301.70 K (Fig. 10a, dark cyan shading), the average θ_v through an equally deep overlying less stable layer is 306.26 K (Fig. 10a, light cyan shading), and thus $\Delta\theta_v = 4.56$ K. Based on these values, $c_{\text{bore}} = 18.5$ m s^{-1} for the near-surface undular bore with mixing. The average wind along the direction of bore motion through the stable layer is −5.63 m s^{-1} (Fig. 10b), giving a ground-relative bore phase speed of 13.5 m s^{-1}, which is near the lower bound of the observation-estimated speed. For the elevated inversion, h_0 = 2460 m AGL (3047 m MSL), h_1 = 3538 m AGL (4125 m MSL), θ_v = 313.19 K, $\Delta\theta_v = 2.63$ K, yielding $c_{\text{bore}} = 18.9$ m s^{-1} for the elevated undular bore with no mixing (Fig. 10a). The average wind parallel to bore motion through the elevated stable layer is −1.42 m s^{-1}, resulting in a ground-relative bore speed of 17.5 m s^{-1} (Fig. 10b), which is 1 m s^{-1} greater than the upper bound of the observation-estimated speed. Bore and solitary wave speeds observed during IHOP ranged ~10–15 m s^{-1}, similar to the features discussed here.

The speed of the bore is greater than that of the MCS cold pool, with this difference visible through an analysis of pod surface station data (Fig. 11). Analysis of the pod data is presented from south to north, following the northeastward propagation of the bore and MCS cold pool. Data collection start times vary for each pod, given that this event occurs during the initial deployment of assets for a later RELAMPAGO IOP. Data are plotted using the same temporal range for all surface pods (0800–1030 UTC) for ease of interpretation. Time series are presented as perturbations from the mean environment, with the mean value calculated at each station location separately using data from the collection start time to 1030 UTC. Perturbations simplify comparisons among stations and avoid potential interpretation complexities due to systematic biases.

Time series data reveal known characteristics of a bore passage (e.g., Koch et al. 1991; Koch and Clark 1999; Koch et al. 2008a,b; Lombardo and Kading 2018; Parsons et al. 2019; Loveless et al. 2019; Lombardo 2020) and cold pool passage (e.g., Fujita 1963; Charba 1974; Goff 1976; Wakimoto 1982; Vescio and Johnson 1992; Engerer and Stensrud 2008). Pod H, the southern-most station, begins collecting data after bore passage, as indicated by radar. Given that DOW7 only begins collecting data at 0830 UTC (Fig. 5a) and DOW8 at 0900 UTC (not shown), the time of the wave passage can only be estimated from the Córdoba Z_H fields (Figs. 2b–d; near 0827 UTC).[3] Bore passages are often defined by an increase in surface pressure. At pod H, the perturbation value (p') rises between 0830 and 0843 UTC (Fig. 11a), within minutes of the estimated time of bore passage over the station. This increase is followed by an oscillating pattern in the perturbation trend,

[3] The influence of pod deployment during the first several minutes or the upstream terrain, given that the surface station is only 6–7 km east of the mountain base, on these perturbation trends cannot be ruled out.

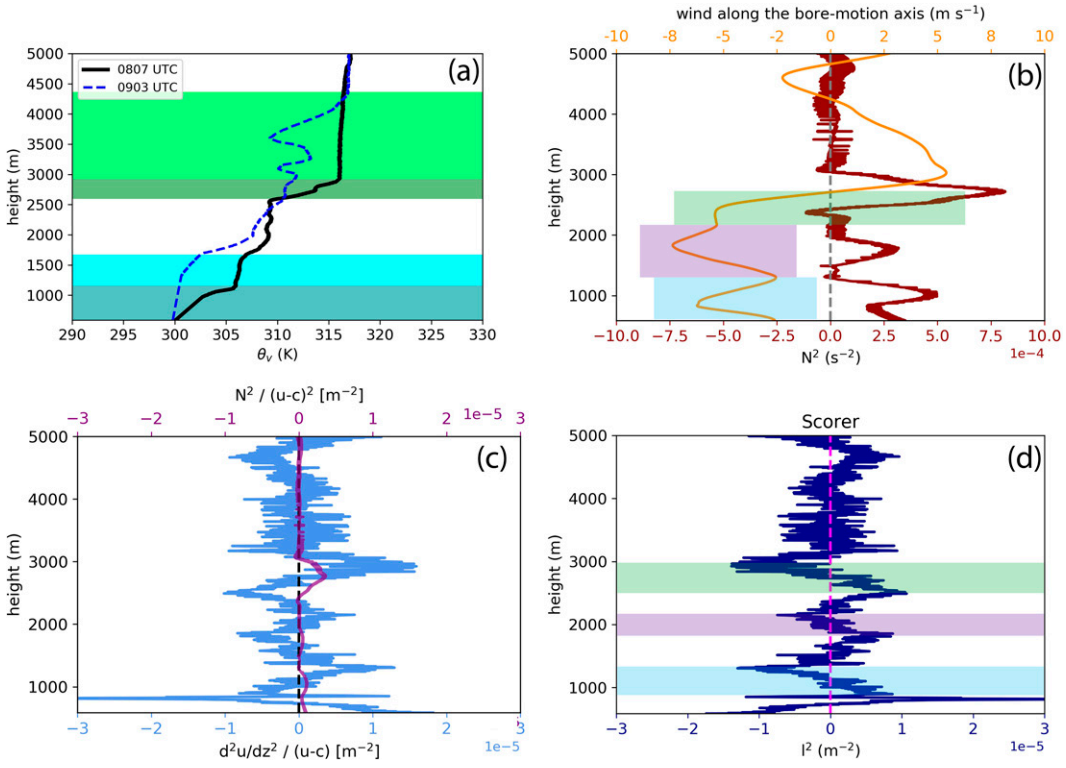

FIG. 10. (a) Vertical profile (m MSL) of virtual potential temperature θ_v based on the UIUC2 0807 UTC sounding (black solid) and UIUC2 0903 UTC (blue dashed). The layer over which h_0 is calculated in the estimation of the theoretical bore speed in Eq. (1) for the lower inversion is shaded dark cyan, and the h_1 layer is shaded light cyan. The layer over which h_0 is calculated in the estimation of the theoretical bore speed in Eq. (1) for the elevated inversion is shaded dark green, and the h_1 layer is shaded light green. The inversion pre- and post-bore heights align with those estimated from the corresponding skew T–log$p$. Vertical profile (m MSL) of UIUC2 0807 UTC (b) N^2 (10^{-4} s^{-2}; dark red) and wind along the axis of bore motion (direction = 59.7°; m s^{-1}; orange), with the three jets opposing bore motion highlighted in blue, purple, and green; (c) the Scorer parameter "stability" term (10^{-5} m^{-2}; purple) and "curvature" term (10^{-5} m^{-2}; light blue); (d) the Scorer parameter (10^{-5} m^{-2}; dark blue), with levels exhibiting a reduction in Scorer parameter shaded in blue corresponding to the blue highlighted jet in (b), purple corresponding to the purple highlighted jet in (b), and green corresponding to the green highlighted jet in (b). The zero lines are indicated with a dashed gray line in (b), black line in (c), and magenta line in (d). A Savitzsky–Golay filter with a third-order polynomial fit and 101 data point window is applied to temperature, moisture, and wind data in (b)–(d).

with a 0.5-hPa decrease between 0843 and 0853 UTC, followed by a 0.5-hPa increase beginning at 0853 UTC. The broader increasing trend in p', which is evident at all pod locations, is associated with changes in the large-scale environment: specifically, a low-level trough exiting the area and the building of a low-level ridge (not shown). The fluctuations observed in the perturbation values are within range of those documented in prior studies, with documented pressure changes ranging between 0.5 and 2 hPa (e.g., Loveless et al. 2019).

The surface perturbation temperature (T') remains effectively constant between 0830 and 0843 UTC, increases 0.5°C between 0843 and 0853 UTC, and decreases 0.2°C between 0853 and 0900 UTC. Surface temperatures have been shown to remain steady, have correlated fluctuations, or have anticorrelated fluctuations with p' during bore passages (e.g., Koch et al. 1991; Loveless et al. 2019). A similar warming was observed during the 27 April 1991 bore event over Oklahoma, due to the downward mixing of air from above the inversion by solitary waves behind the bore (Koch and Clark 1999; Koch et al. 2008b). This surface warming is consistent with the presence of the near-surface undular bore with turbulent mixing and the h_1/h_0 = 2.57 relationship calculated above (Rottman and Simpson 1989). Surface warming is also evidence that the feature causing these thermal perturbations is not the cold pool of the parent MCS. Magnitudes of T' are consistent with those observed in prior studies, as well, with documented temperature changes often <1°C following bore passage (e.g., Loveless et al. 2019). Water vapor mixing ratio perturbations (q'_v) have been shown to either increase or decrease upon passage; here, values decrease at pod H until ~0840 UTC, consistent with vertical mixing behind the bore head, and then remain steady until ~0900 UTC.

A more dramatic change in T' and q'_v begins near 0900 UTC as the parent MCS cold pool passes over the station. The

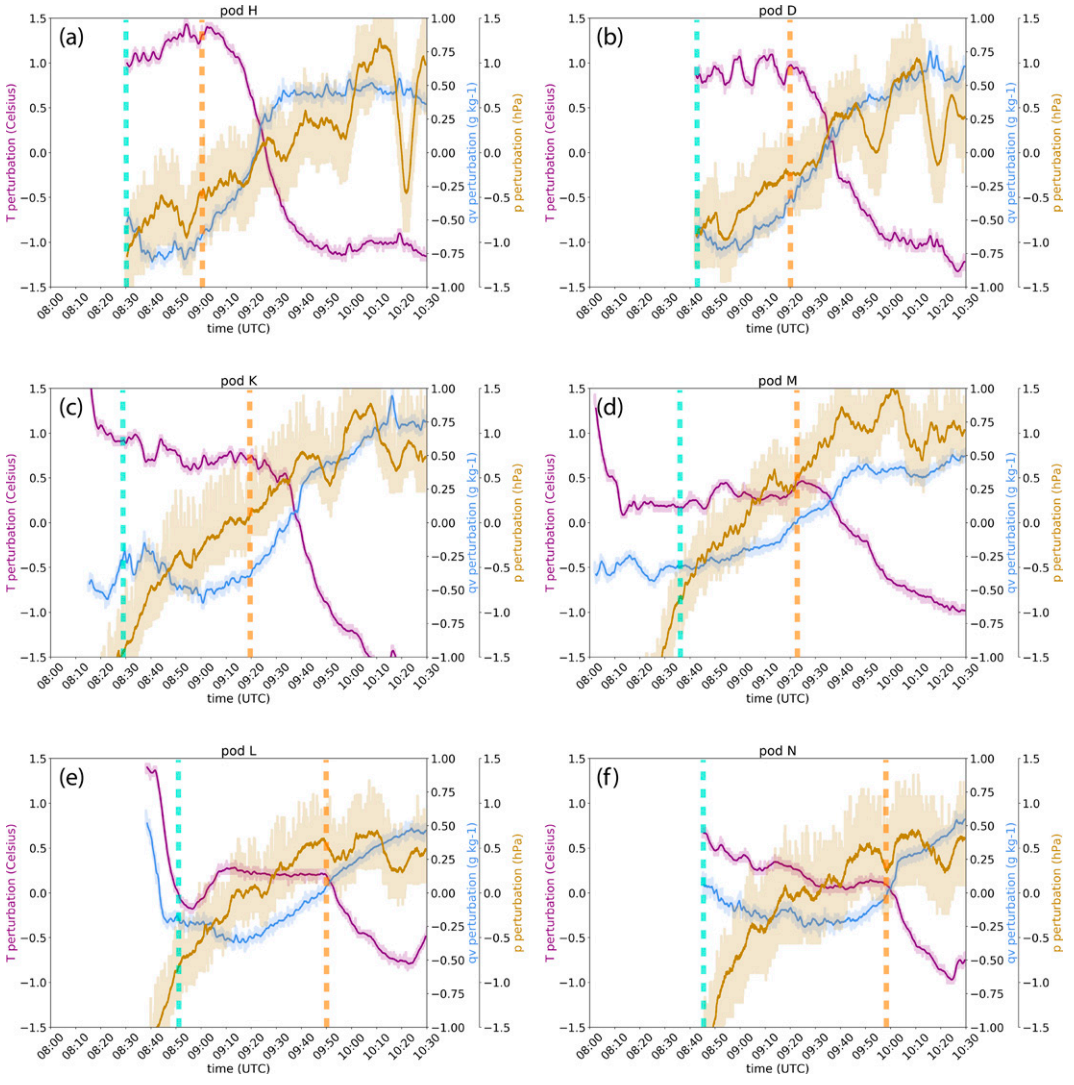

FIG. 11. Time series of surface perturbation temperature (T'; °C; purple), perturbation water vapor mixing ratio (q_v'; g kg^{-1}; blue), and perturbation pressure (p'; hPa; gold) at (a) pod H from 0830 to 1030 UTC, (b) pod D from 0842 to 1030 UTC, (c) pod K from 0815 to 1030 UTC, (d) pod M from 0802 to 1030 UTC, (e) pod L from 0838 to 1030 UTC, and (f) pod N from 0845 to 1030 UTC. Shading shows perturbations from the mean value averaged over the time period illustrated in the time series, and solid lines are the 1-min moving average perturbation values. Teal dashed lines indicate passage of the bore, and orange dashed lines indicate passage of the MCS cold pool. Teal dashed lines at the beginning of the time series indicates that data collection occurred after the bore passage. See Fig. 1 for station locations.

close proximity of the surface station to the parent MCS at this time is visible in Fig. 6d. A 2.25°C decrease in T' and 2 g kg^{-1} increase in q_v' occurs over a 30-min period, while p' steadily increases (Fig. 11a). The bore is located northeast of pod H during this time (Fig. 5d).

Eight kilometers to the north, at pod D, data collection also begins soon after the leading edge of the bore propagates over the station. Bore passage results in correlated oscillations in p' and T', with a simultaneous increase between 0840 and 0850 UTC, decrease between 0850 and 0855 UTC, and increase until 0900 UTC (Fig. 11b). Though p' steadily increases after this time, fluctuations in T' continue, indicating the presence of additional trailing gravity waves and their associated vertical turbulent mixing behind the undular bore front. The q_v' generally decreases from 0843 to 0850 UTC, with a notable increasing trend after 0900 UTC (Fig. 11b). The trailing MCS cold pool moves over pod D at 0920 UTC (Fig. 11b), ~15 min later than at pod H to its south. Passage of the cold pool is progressively later for pods farther north (Figs. 11c–f). Estimated from pod data, the cold pool speed is ~10 m s^{-1}, notably slower than the observed and calculated speed of the bore.

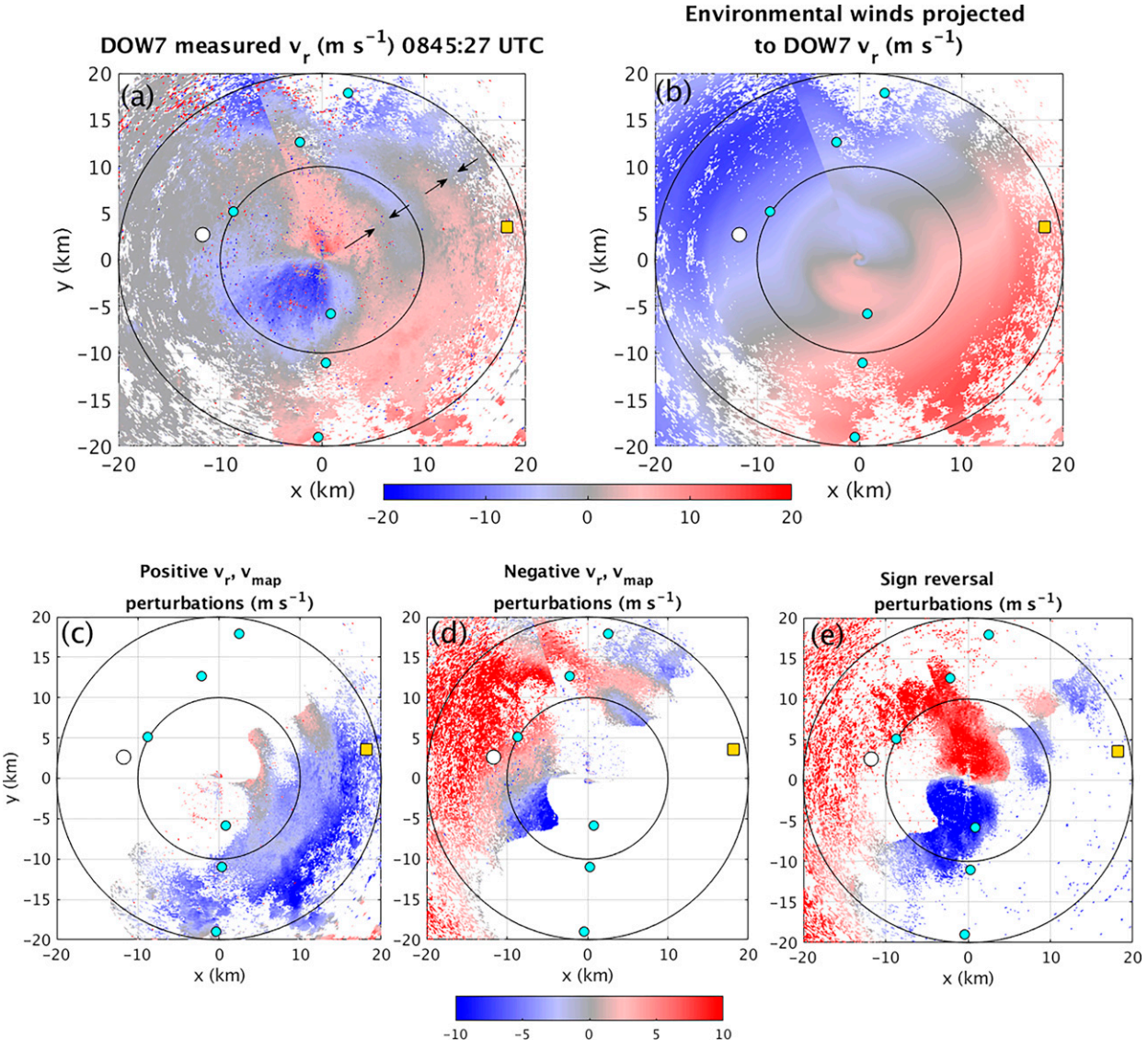

FIG. 12. DOW7 5.5° PPI scan of radial velocity (v_r) at 0845 UTC 5 Nov 2018. Black arrows indicate regions of radial convergence. (b) Environmental winds from the UIUC2 0832 UTC sounding projected onto DOW7 v_r, referred to as v_{map} in the text. (c) Perturbations (defined as the difference $v_r - v_{map}$) for when v_r and v_{map} are both positive; (d) perturbations for when v_r and v_{map} are both negative; and (e) perturbations for when v_r and v_{map} are of opposite sign. In all panels, 10- and 20-km range rings are overlaid. Velocities are shaded according to scale in m s^{-1}; note the color scale differences in the top row and the bottom row. The conversion of the sounding-observed u and v to v_{map} follows geometric considerations in, for example, Browning and Wexler (1968) and Kumjian and Lombardo (2017).

6. The role of bores in convection initiation

a. *Localized convergence and ascent*

Prior studies have illustrated that bores and their trailing waves, if present, are associated with lines of convergence (Koch et al. 2008a,b; Haghi et al. 2017; Grasmick et al. 2018), and thus provide a mechanism to initiate convective cells. For example, inbound and outbound oscillations were observed in the WSR-88D radial velocity data for a bore and several trailing gravity waves in the wake of the bore moving over Des Moines, Iowa, which had horizontal wavelengths of ~8 km (Coleman et al. 2010). DOW7 5.5° v_r data provide evidence of such convergence boundaries associated with the bore and trailing waves during our discrete propagation event, marked by a periodic reversal in wind direction. Figure 12a shows the DOW7 radial velocities (v_r) measured at 0845 UTC, at 5.5° elevation angle. This elevation angle was chosen to avoid the more severe low-level beam blockage (cf. Fig. 5). At this time, the boundary has passed the DOW7 location, as evidenced by the strong (>10 m s^{-1}) southerly flow at DOW7. Between ~5- and 10-km range, to the northeast of DOW7, a band of radial convergence is evident as outbound v_r transitions to

inbound v_r. The beam height in this region is between about 0.5 and 1.0 km AGL, assuming standard atmospheric refraction (e.g., Doviak and Zrnić 1993), and thus located below the top of the elevated inversion. Just beyond this convergence band, a divergence band is observed as the inbound v_r transitions to zero and slightly outbound v_r. Though this pattern of alternating convergence and divergence is consistent with the presence of a bore and trailing waves, vertical wind shear can also lead to these types of patterns in v_r data.

To examine these possibilities, we mapped the horizontal winds from the 0832 UTC UIUC1 sounding (~27 km northwest of DOW7, 13 min before the scan) as if they were DOW7 radial velocities (Fig. 12b). We will refer to these projected velocities as v_{map}. Here, vertical wind shear in the lowest 2 km AGL solely is responsible for the changes in v_{map} in Fig. 12b. To facilitate comparison with the DOW7-measured v_r, pixels with no data are censored from both panels.

Figures 12c–e show the difference between the DOW7 v_r measurements and the sounding-projected v_{map}; for ease of interpretation, the difference plots are divided into those in which v_r and v_{map} are both positive (Fig. 12c), both negative (Fig. 12d), or of opposite sign (Fig. 12e). In Fig. 12c, at a range of about 5 km, a region of positive $v_r - v_{\text{map}}$ differences extends from east to northeast of DOW7; radially outward from this region, these differences become zero, and then negative. This implies that the DOW7-observed radial winds are more outbound (a positive perturbation) and then less outbound (negative perturbation) than the environmental winds, with increasing range from the radar. This highlights a band of convergence in the perturbations, suggesting the radar detects more convergence in this PPI scan than what would be expected from the environmental wind profile alone. A similar pattern exists farther to the northeast, near ~12–13-km range, and again suggests a convergent perturbation in the flow. These convergence perturbations are separated by roughly 7–8 km, which is consistent with the wavelengths estimated from RMA1 Z_H PPI data (8.2 ± 1 km), and consistent with prior studies.

Figure 12d shows the perturbations when v_r and v_{map} are both negative. A region of negative perturbations begins near the 10-km range ring to the northeast of DOW7, which implies more negative (more inbound) velocities than would be expected from the environment alone. Radially just beyond this region (12–13-km range), positive values suggest less negative (less inbound) velocities. Together, these mark a region of perturbation divergence (i.e., more divergent than the environmental flow alone), situated between the two regions of perturbation convergence inferred from Fig. 12c. Another region of negative values is found between 16- and 17-km range; combined with the radially inward region of positive values, this implies convergence. Collectively, these are consistent with bore and trailing wave characteristics superposed on the background flow, with a wavelength on order of 7–8 km.

Figure 12e shows perturbations where the v_r and v_{map} are of opposite sign. The most prominent feature in this panel is the strong dipole centered on the radar, which arises owing to the wind shift to strong southerlies associated with the bore passage (Figs. 7d,e). The region of positive perturbations in Figs. 12d and 12e to the west of DOW7 arise owing to ground clutter from the higher terrain (where environmental winds should be observed as inbound, but the ground clutter contamination renders these velocities near zero). Northeast of DOW7, perturbations with alternating signs can be seen as spatial continuations of the patterns observed in Figs. 12c and 12d (i.e., plotting the three panels together reveals a coherent pattern in this region).

Further evidence that these v_r features in DOW7 measurements are from a bore and trailing waves is found by inspecting the consecutive scans through this period (Fig. 13). The series of images shows the patterns in the v_r field moving northeastward during the 10 min shown, which is more consistent with a propagating feature perturbing the lower-tropospheric flow than rapid changes to the lower-tropospheric background wind profile. Thus, collectively, the DOW7 v_r data provide strong evidence of a bore and trailing waves propagating northeastward during this time.

As the bore and trailing waves propagate northeastward, it becomes more challenging to identify these wind reversals due to the development of the isolated cells and increased distance from DOW7. However, there is evidence that the cells initiate along linear bands, parallel with the observed convergence lines (Fig. 14). Therefore, one may hypothesize that CI occurs in association with multiple lines of ascent associated with the bore and waves. Viewing the deepest convective cells more clearly highlights the connection between cell development and the convergence boundaries (Fig. 14), though these CI patterns are evident in data from lower radar scan angles, as well (Figs. 6b,c). At 0841 UTC, as the field of cells develops (Figs. 3b and 6b), CI occurs along two separate, parallel lines with spacing of about ~9–10 km (Fig. 14a). As the cells mature and as more initiate along the existing lines, the bands move northeast in the same direction of the bore motion (Fig. 14b). Over time, an additional band of cells becomes visible with similar 9–10-km spacing (Fig. 14c), suggesting the presence of a third convergence boundary. The bands of isolated cells merge as the system undergoes the discrete propagation and the cells grow upscale (not shown).

b. *Modification to the environment by the bore*

As the bore moves faster than and ahead of the MCS cold pool, it modifies the environment in its wake (Table 2), as illustrated by the 0903 UTC UIUC2 sounding (Fig. 7d). The observed environmental evolution during bore passage aligns well with observations of bore-modified environments documented in the literature. Bores have been shown to create more a favorable environment for deep convective storm initiation in their wake (Koch et al. 2008b; Parsons et al. 2019; Zhang et al. 2020). During IHOP, bores generated by nocturnal MCSs were observed to induce a net upward displacement as large as 800–900 m, lifting air within the stable layer as well as air within the conditionally stable layer above (Parsons et al. 2019). This lifting reduced the ambient SBCIN, and aided in the development of new convective cells behind the bore. Similar processes were observed during a nocturnal elevated MCS event during PECAN (Grasmick et al. 2018); bore-induced ascent lifted air within the residual

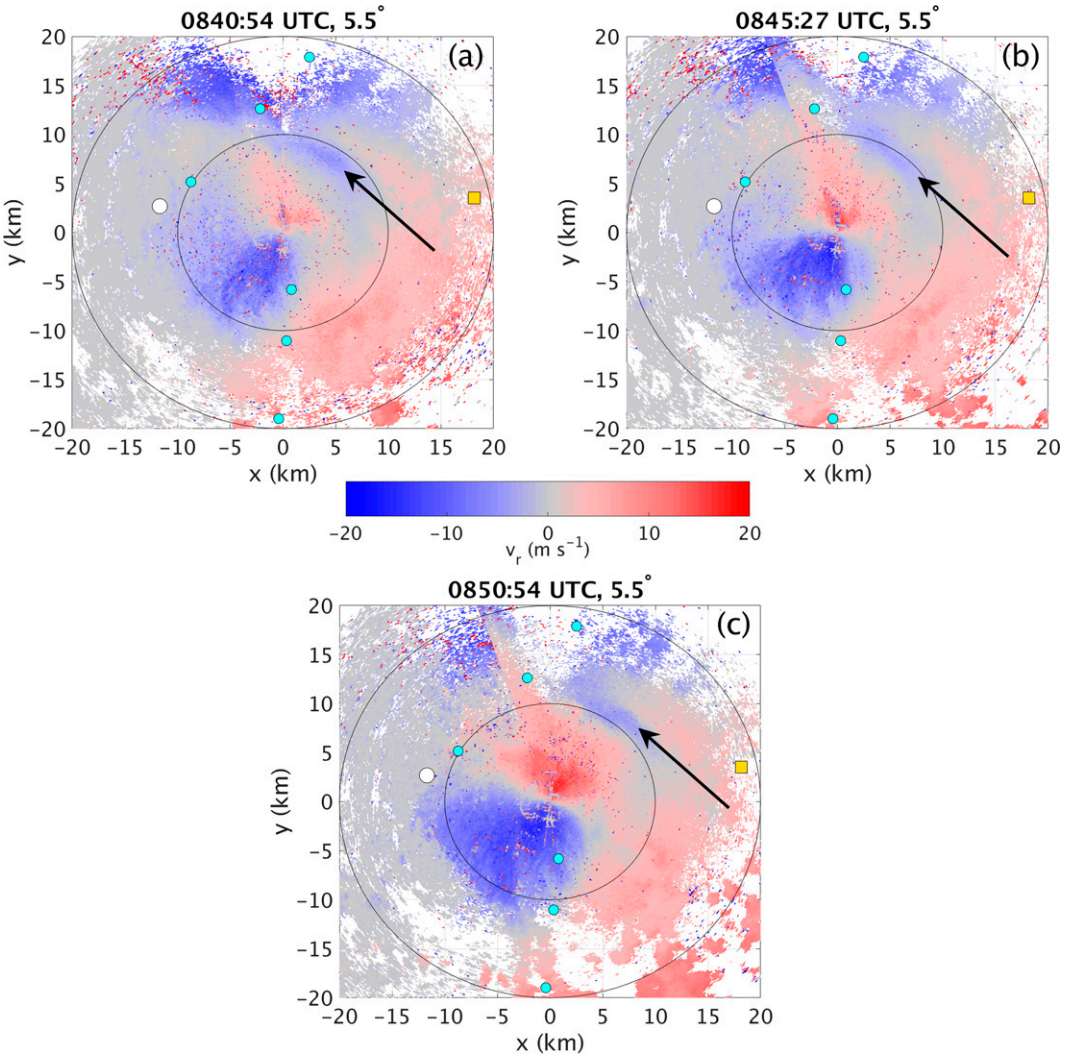

FIG. 13. (a) DOW7 5.5° PPI scans of radial velocity (v_r) at (a) 0840:54, (b) 0845:27, and (c) 0850:54 UTC 5 Nov 2018. In all panels, 10- and 20-km range rings are overlaid. Velocities (m s^{-1}) are shaded according to scale. Black arrows highlight the movement of the inbound component of one convergence line.

mixed layer overlying the nocturnal inversion as much as 1 km, which reduced SBCIN to near zero and supported CI in its wake.

For our Argentine MCS, bore-driven ascent cools and moistens air within and above the stable layers. This cooling reduces the magnitudes of the capping inversions and decreases the environmental SBCIN/MUCIN (Table 2; Fig. 7d). The magnitudes of the vertical displacements for the near-surface and elevated inversions, 860 and 1078 m, respectively, are consistent with prior bore studies. The altitude of the most-unstable parcel in the pre-bore environmental soundings is located at the apex of the elevated inversion (Table 2; Figs. 7a–c). Bore-driven ascent increases the height of this inversion from 2460 to 3538 m AGL. Given the deep layer lifting and small MUCIN for these parcels, these elevated parcels rise freely and contribute to CI. The height of the near-surface inversion increases to 1388 m AGL, below the height of the surface-based LFCs (Table 2), indicating that surface-based parcels are likely not contributing to CI. However, both inversions remain elevated at least 30 min after the bore moves over UIUC2, and this semipermanent deepening of the boundary layer is characteristic of bore passages (e.g., Parsons et al. 2019; Weckwerth et al. 2019).

Data from the vertically pointing DIAL offer a complementary view of the vertical displacement of the low levels and provide additional insight into the temporal relationship between bore passage and CI. DIAL data illustrate variability in boundary layer water vapor density and highlight the presence of clouds (Fig. 15a). Given the strong increase in lidar backscatter in regions of cloud droplets, backscatter can be used to determine cloud base altitude (Fig. 15b; Kotthaus et al. 2016). Thus, the data can be used to track the movement of the propagating bore and trailing waves, including the timing of cell initiation with respect to bore passage. Note, absolute

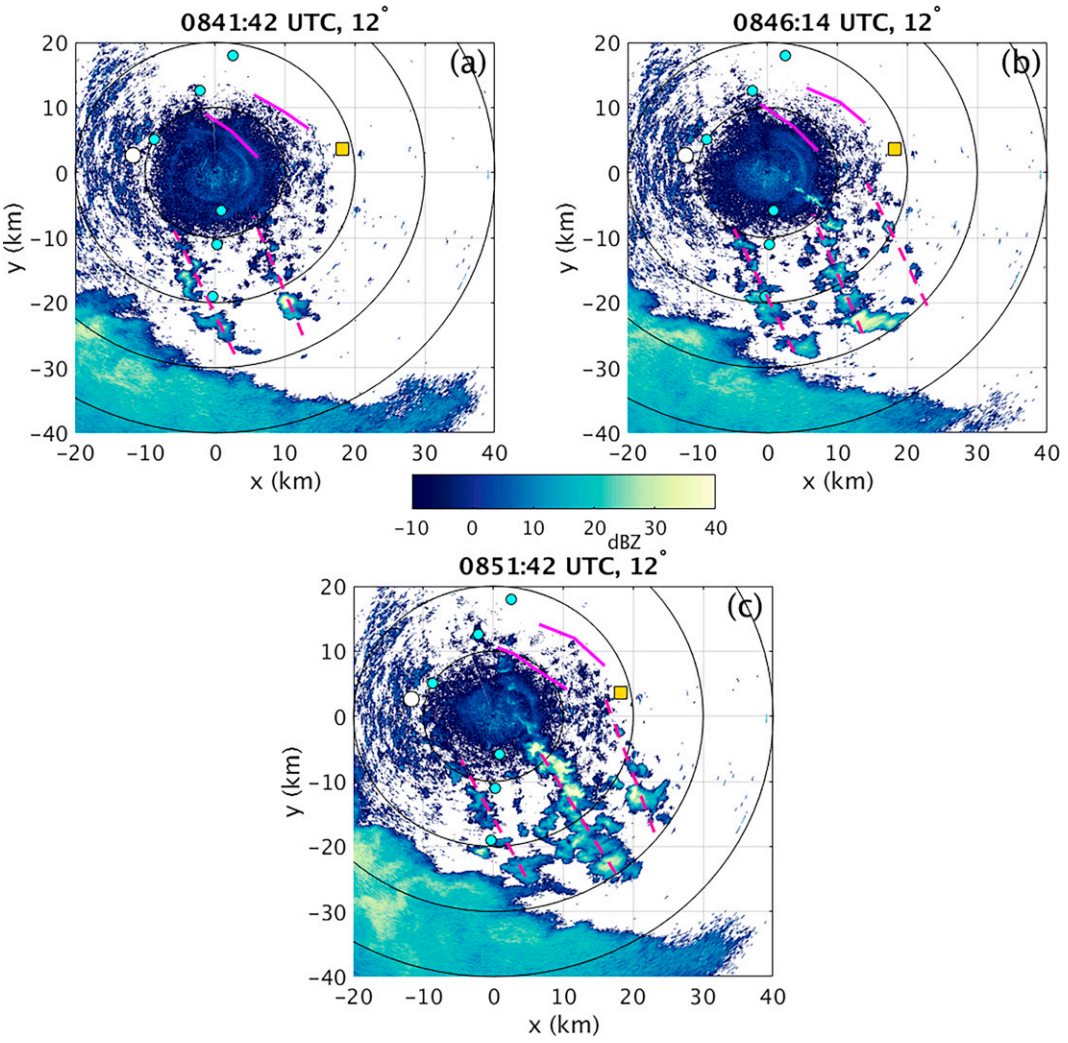

FIG. 14. DOW7 11.9° PPI scans of Z_H at (a) 0841:42, (b) 0846:14, and (c) 0851:42 UTC 5 Nov 2018. The magenta dashed lines annotate the lines of initiating convective cells; the magenta solid lines indicate the approximate locations of convergence boundaries identified in Fig. 13.

humidity values within the cloud (>18 g m^{-3}) are masked white due to the large attenuation of the lidar beam in optically thick clouds and the unreliability of the data in these regions (Weckwerth et al. 2016). The UIUC2 thermodynamic profile observed at 0807 UTC supports the DIAL determination of cloud-base level, with relative humidity values exceeding 80% above 1.43 km, and 90% above 1.66 km (Fig. 7a).

Between 0900 and 0930 UTC, DIAL time series data show notable oscillations in cloud-base height, highlighting the passage of the bore and the initial trailing wave (e.g., Koch et al. 2008b; Haghi et al. 2019). Cloud-base height increases from 1232.9 to 1495.2 m MSL (899.9–1162.2 m AGL; Δz = 262.3 m) between 0900 and 0910 UTC during the passage of the bore, based on the vertical displacement of the bottom of the layer of high backscatter (Fig. 15b). Following this ascent, cloud base descends to 1382.8 m MSL by 0913 UTC. Passage of the initial trailing gravity wave causes the cloud base to ascend again to 1570 m MSL (Δz = 187.2 m; a smaller displacement than during bore passage) by 0916 UTC. Note that the passage of the gravity wave is associated with a decrease in boundary layer vapor density (Fig. 15a), consistent with vertical mixing by trailing waves and the increase in surface temperature (Figs. 11a,b). The multiple, sequential increases in cloud base height are consistent with the presence of several convergence boundaries visible in DOW7 v_r and multiple fine lines in the RMA1 Z_H. Further, the timing of bore passage as observed by the DIAL is consistent with the timing of passage of the RMA1 fine lines over the DIAL location. The fine lines are detectable by RMA1 until 0845 UTC (Fig. 9e). At this time, the leading fine line is located approximately 10 km to the west-southwest of the DIAL location. Assuming the bore moves at 13–16.5 m s^{-1}, it is estimated to pass over the DIAL location within approximately 10.1–12.8 min, between 0855 and 0858 UTC, consistent with the timing of the DIAL-

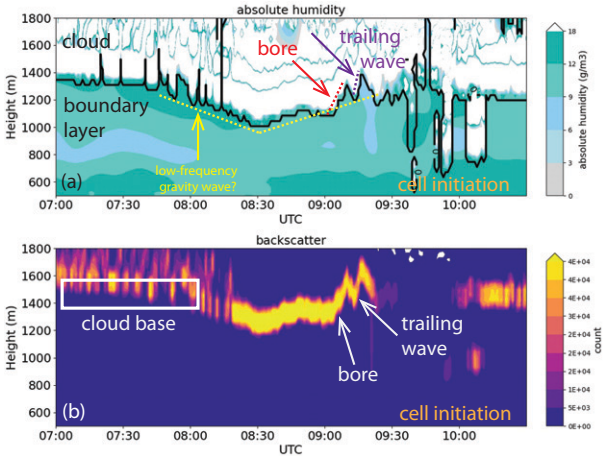

FIG. 15. Differential absorption lidar observations from 0700 to 1030 UTC of (a) absolute humidity (g m^{-3}; shaded), and (b) post-processed backscatter (arbitrary units). The black line in (a) is the delimiter between data with no cloud mask (essentially the cloud-free boundary layer) and data with a cloud mask applied (essentially the optically thick cloud). Values of absolute humidity in regions of cloud are ignored due to the heavy attenuation of the radar beam. The shading interval was selected to de-emphasize these regions, with values above 18 g m^{-3} shaded white. Height is in meters MSL.

observed increase in cloud-base height. After bore and wave passage, isolated convective cells form over the DIAL between 0930 and 1030 UTC, visible in both the moisture fields (Fig. 15a) and RMA1 Z_H PPI (Figs. 2g,h). The cloud-base height remains elevated, consistent with the semipermanent lifting of the inversion layers (Figs. 7d,e).

Unlike other observational platforms deployed during this event, the DIAL begins sampling the environment several hours prior to bore passage and thus, the data provide insight into variations in the environment well before the MCS discrete propagation. Prior to bore passage (0700–0800 UTC), cloud base height is relatively constant near 1.5 km (Fig. 15b), and boundary layer water vapor density ranges between 6 and 18 g m^{-3} (Fig. 15a). Between 0800 and 0830 UTC, cloud base lowers to ~1250 m MSL, and the vapor density through the boundary layer becomes more uniform, with moistening between 700 and 1000 m. The mean height of the cloud base ascends again from 0830 to 0920 UTC, potentially superposed over the cloud-base height oscillations associated with the bore and trailing gravity wave. This transition is reminiscent of the descent and ascent associated with a low-frequency gravity wave generated from deep convection. Latent heating associated with MCS precipitation is known to generate multiple gravity waves with a broad range of wavelengths and spectral peaks (Lane and Reeder 2001; Alexander and Holton 2004). The vertical motion associated with gravity waves of different frequencies will manifest within the troposphere distinctly, and thus have the potential to modify the tropospheric environment in different ways. Convectively generated low-frequency $n = 1$ waves exhibit tropospheric deep ascent or descent, whereas $n = 2$ waves produce a vertically stacked couplet of vertical motion through the troposphere, i.e., low-level ascent overlying upper-level descent or vice versa (Nicholls et al. 1991; Mapes 1993; Fovell 2002). Lower-tropospheric ascent associated with $n = 2$ waves has been shown to cool and moisten the low-levels, thereby reducing static stability within the layer and creating an environment favorable for CI (Fovell 2002; Fovell et al. 2006).

We look for additional evidence of low-frequency wave passage in the sounding data. Given the direction of motion of the MCS, we anticipate a low-frequency wave to pass over the DIAL and UIUC sounding location at similar times. Comparison of UIUC1 0832 UTC and UIUC2 0903 UTC provides insight into the changing environmental conditions during cloud-base ascent. The largest temperature difference occurs below 4510 m MSL (589.5 hPa), with an average cooling of −2.3°C through the layer from the surface to 4510 m. One would associate the increase in cloud-base height with descending motion and the associated warming and drying from a tropospheric wave, rather than the cooling observed here. In the upper troposphere, there is a shallow layer of warming near 6000 m, underneath a layer of cooling above 7000 m, with an average temperature change through 4515–9375-m layer of only −0.1°C.

In general, evidence of low-frequency gravity wave passage in inconclusive. Perhaps this is not surprising, given the presence of the mountains, which may modify existing convectively generated waves and may be responsible for the development of additional waves as the midlevel flow passes over the barrier. Further, Groff et al. (2021) noted the tropospheric response to $n = 2$ waves may become "hidden" among the response to other convectively generated low- and high-frequency waves, with such responses sensitive to the presence of a surface-based nocturnal stable layer and tropospheric vertical wind shear.

7. Environment to support bore and trailing waves

To support our assertion that a bore and trailing gravity waves are responsible for the discrete propagation of the MCS, we diagnose the ambient conditions to assess the presence of an environment supportive of both phenomena. Studies have shown that the most important feature to support bore maintenance within a stable layer is the presence of a jet opposing the motion of the bore (Doviak and Ge 1984; Crook 1988; Fulton et al. 1990; Haghi and Durran 2021). Figure 10b illustrates the vertical profile of wind along the axis of bore motion, based on the UIUC2 0807 UTC vertical profile. Winds oppose bore motion from the surface to 2710 m, with three individual vertically localized jets within the broad layer. The altitude of a near-surface jet (Fig. 10b, blue shading) overlaps with that of the near-surface stable layer (Fig. 10a, blue shading), while the altitude of the elevated jet (Fig. 10b, green shading) overlaps with that of the elevated stable layer (Fig. 10a, green shading). A third jet located between the two (Fig. 10b, purple shading) is at a similar altitude to a weakly stable layer located between 1500 and 2000 m. (Fig. 10a). Thus, conditions appear favorable to support the lateral propagation of a bore within several lower-tropospheric

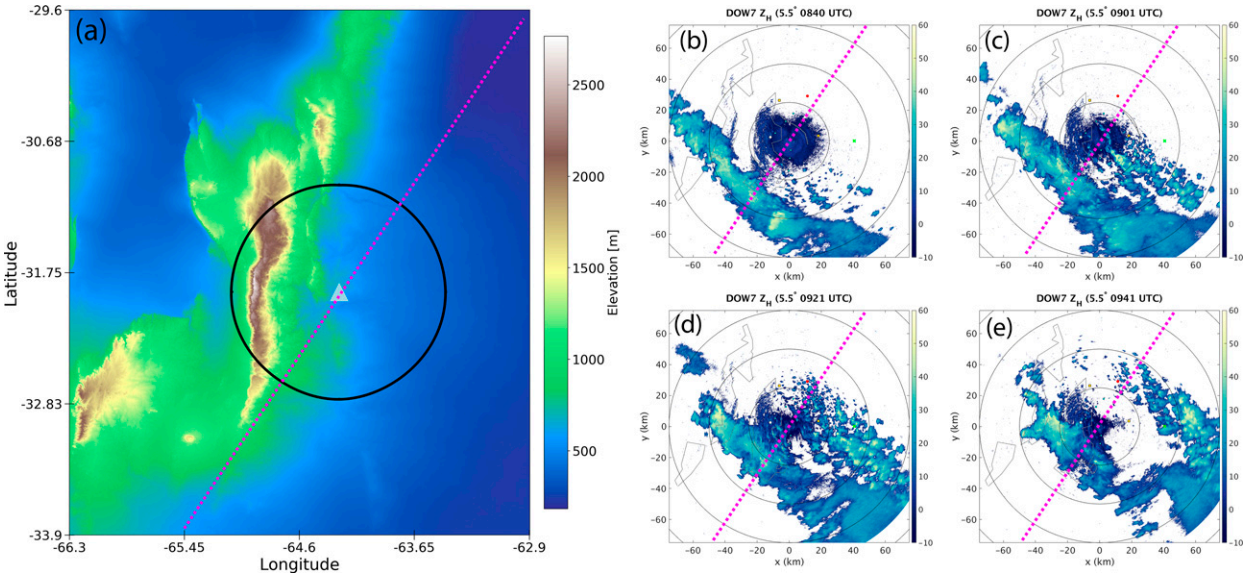

FIG. 16. (a) Terrain map of the Sierras de Córdoba, including the location of DOW7 (light blue triangle) and approximate location of DOW7 75-km range ring (solid black line circle) and (b)–(e) the outer range rings. DOW7 5.5° PPI of Z_H at 0840, 0901, 0921, and 0941 UTC 5 Nov 2018 in (b)–(e), respectively. Range rings are marked in 25-km intervals. The magenta dashed line marks the orientation of bore movement across the domain in all panels.

stable layers. Similar results are found using UIUC1 0832 UTC data (not shown).

The Scorer parameter $\ell^2(z)$ (Scorer 1949; Crook 1988) is often used to assess the ability of the atmosphere to vertically trap energy associated with gravity waves (Lindzen and Tung 1976; Fovell et al. 2006; Koch et al. 2008b; Coleman et al. 2010; Haghi et al. 2017) allowing for their lateral movement.[4] The Scorer parameter comprises two terms:

$$\ell^2(z) = \frac{N^2}{(U-c)^2} - \frac{\frac{\partial^2 U}{\partial z^2}}{(U-c)}, \tag{2}$$

where N is the Brunt–Väisälä frequency, U is the environment wind parallel to the direction of wave front movement, c is the speed of the wave, and z is the vertical distance. The first term on the RHS is often considered a "stability" term given its dependence on N^2, and the second term on the RHS is considered a "vertical wind shear" or "vertical wind curvature" term due its dependence on $\partial^2 U/\partial z^2$. We evaluate the Scorer parameter using data from the UIUC2 0807 UTC sounding (Fig. 10), including individual terms in the equation; values are similar for UIUC1 0832 UTC (not shown). Figure 10b illustrates the vertical profile of N^2 and U used in the calculation of $\ell^2(z)$. As expected, N^2 is relatively large within the inversion levels, with maxima ranging between 2.5×10^{-4} and 7.5×10^{-4} s^{-1}. Figure 10c illustrates the vertical profile of the Scorer parameter stability term (purple) and the curvature term (blue) for $c = 16$ m s^{-1}. (Results are insensitive the range of c values observed and calculated in this study; specifically, $c = 13$ and 17.5 m s^{-1} were tested.) The curvature term dominates the resulting Scorer parameter, as in Haghi et al. (2017), for example.

Figure 10d illustrates the total Scorer parameter within the lower atmosphere. A reduction of the Scorer parameter with height suggests conditions are favorable for gravity wave trapping, and for layers in which $\ell^2(z) < 0$, all waves originating from below the layer are vertically trapped (e.g., Crook 1988; Fovell et al. 2006; Koch et al. 2008b; Coleman et al. 2010; Grasmick et al. 2018; Haghi and Durran 2021). Here, there are three levels in which $\ell^2(z)$ decreases with height, and in fact $\ell^2(z)$ falls below zero, corresponding to the levels of relatively high static stability and curvature in the vertical wind profile, indicating conditions are favorable to trap the trailing gravity waves behind the leading bore.

8. Role of the Sierras de Córdoba

The Sierras de Córdoba influence the discrete propagation of the MCS in two ways: 1) "confine" the low-level stable layer to mountain lee, 2) prevent the northern segment of the MCS from propagating discretely. First, the top of the low-level inversion as observed by the UIUC and Córdoba soundings (Figs. 7a–c) prior to bore passage is located at ~540 m AGL, which is below the height of much of the mountain chain (Fig. 16). Given that the surface level of the sloping terrain to the west is located above the top of the nocturnal near-surface inversion, the inversion was likely localized east of the mountains, though a lack of soundings from over the

[4] Haghi and Durran (2021) argue that one must solve the eigenvalue eigenfunction to definitely determine the ability of an environment to support trapped waves.

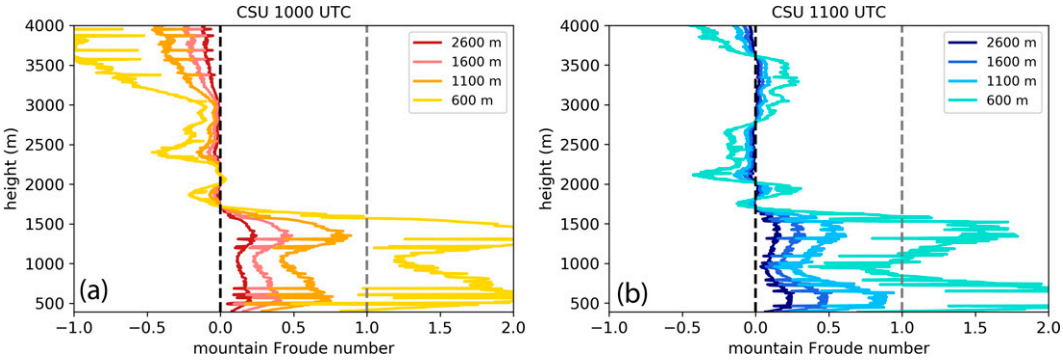

FIG. 17. Vertical profile of the mountain Froude number calculated using cold-pool-perpendicular winds for the (a) CSU 1000 UTC sounding for a mountain height of 2600 m (dark red), 1600 m (pink), 1100 m (orange), 600 m (yellow), and (b) CSU 1100 UTC sounding for a mountain height of 2600 m (dark blue), 1600 m (blue), 1100 m (light blue), and 600 m (turquoise).

sloping terrain and from points farther south prevents evaluation of this hypothesis. Second, the bulk of the convective redevelopment occurs over and to the south of the deployed assets due to variability in the height of the mountain peaks along the north–south-oriented chain. Figure 16 highlights the evolution of the MCS with respect to the local terrain and the orientation of the bore motion (magenta dashed line). Following the motion of the bore, the discrete propagation occurs to the right (southeast and east of DOW7), with minimal cell development to its left (northwest and north of DOW7). The height of the mountain peaks underlying the portion of the MCS that propagates discretely (southeast of the magenta line) are below 1000 m, whereas mountain peaks are at least 2000 m tall along much of the mountain ridge underlying the portion of the MCS that fails to propagate discretely (northwest of the magenta line). We hypothesize that the parent MCS cold pool is disrupted by the high terrain as it attempts to traverse the mountains. Thus, the cold pool is unable to perturb the leeside stable layer in this region and initiate a downstream bore which is necessary for the discrete propagation.

Often, the ability of an MCS cold pool to traverse a mountain ridge is evaluated using a nondimensional parameter that combines the impacts of ambient stability and wind, called the mountain Froude number, $F_r = U/Nh$, where U is the base-state wind, N is the Brunt–Väisälä frequency, and h is the mountain height (Long 1972; Baines 1979; Smith 1979; Pierrehumbert and Wyman 1985; Chu and Lin 2000). Low Froude number environments (typically below 1) are characterized as blocked flow regimes in which MCS cold pools are unable to cross the mountain ridge, whereas high Froude number environments (typically near or larger than 1) are considered unblocked flow regimes that favor cold pool mountain crossing (Chu and Lin 2000; Frame and Markowski 2006; Reeves and Lin 2007). Mountain F_r values are typically evaluated for the environment upstream of the mountain, though a lack of sounding data from this region prevents such analysis for this event. Thus, we are constrained to calculate F_r using downstream vertical profiles. The following discussion is based on the assumption that the environment upstream of the mountain resembles the environment downstream of the mountain.

The vertical profile of mountain F_r is calculated for two environments: the environment prior to cold pool passage (CSU 1000 UTC) and the environment following cold pool passage (CSU 1000 UTC). Values are calculated for four different mountain heights: two representative of mountain peaks along the northern portion of the Sierras de Córdoba (2600, 1600 m) and two representative of mountain peaks along the southern portion of the Sierras de Córdoba (1100, 600 m). Values are calculated for the environment before and following cold pool passage, since F_r has been shown to change following the development of a cold pool by local convection. For example, Reeves and Lin (2007) illustrated the transition from an unblocked to a blocked flow regime due to the development of a cold pool associated with a MCS located over the windward slopes of the mountain. Given the southeast–northwest orientation of the MCS and its northeastward movement (Figs. 2a–c), we assume the cold pool moves to the northeast, as well, and thus we calculate F_r using winds along the axis of motion of the MCS cold pool. We use $F_r = 1$ as an approximate threshold between flows that are more likely to become blocked by the mountain ($F_r < 1$) versus those that are more likely to crest the terrain ($F_r > 1$), though we recognize that this is not a precise threshold value for prediction and should be considered a continuum. Further, cold pools may become partially blocked by terrain, during which only a shallow layer of the negatively buoyant air successfully moves over the mountain rather than the full depth of the cold pool (e.g., Frame and Markowski 2006; Reeves and Lin 2007). Below 1750 m in altitude, $F_r > 1$ both prior to (Fig. 17a, yellow line) and following (Fig. 17b, green line) cold pool passage for mountain height peaks below 600 m, suggesting flows from the surface to 1750 m are able to traverse the shorter mountain peaks along the southern Sierras de Córdoba. At both times, flows are increasingly likely to be blocked by progressively taller terrain peaks, with F_r values approaching 0.1 for

mountain peaks of 2600 m. Above 1750 m altitude, F_r values fall below 0.

Radiosondes released from the southern-most mobile unit (CSU) provide insight into depth of the MCS cold pool after it traverses the lower mountain peaks; note, CSU is located southeast of the dashed magenta line in Fig. 16. At 1000 UTC, a shallow (268 m deep) surface-based inversion is visible at the CSU mobile site (Fig. 7f), with a surface temperature 1°C lower than observed 1 h earlier (Fig. 7e). This may be the remnants of the cold air generated by the cells involved in the discrete propagation (Figs. 6e,f), given that no precipitation is located over the site at this time (Fig. 6j). This may also be evidence of the parent MCS cold pool just beginning to move over the CSU launch site; given the orientation of the cold pool, we expect that it moves over pod N and the CSU mobile unit at a similar time, ~1000 UTC. By 1100 UTC, the cool layer deepens to 1113 m (Fig. 7g), as low-level winds through the layer rotate counterclockwise to southerly. This reflects the passage of the trailing cold pool of the parent MCS, indicating that the cold pool is approximately 1.1 km deep in the mountain lee. Intuitively, the taller mountain peaks have the potential to limit or prevent the passage of a cold pool of this depth. We should note, however, it is unclear whether the cold pool had a similar depth while over the windward side of the mountain, or if a portion of the cold pool was blocked by the mountain, resulting in a shallower leeside depth. For example, the more moderate peaks of the Sierras Grandes (1000–1500 m) may have partially blocked the cold pool, allowing only *some* of the cool outflow to traverse the mountain, while the northern peaks of the Sierras Grandes, which approach 2600 m, in combination with the downstream 1200 m peaks of the Sierras Chicas (Fig. 1) may mostly or completely block the MCS cold pool.

The impact of the mountains on bore development is also evident in the surface pod data (Figs. 11c–f). Bore passage over pod K (~5 km north of pod D) is estimated to occur at 0827 UTC, based on radar data;[5] however, it is challenging to identify the passage of the bore in the trace of p' (Fig. 11c). The increasing trend in p' is relatively constant following bore passage rather than exhibiting a temporally localized increase followed by a decrease, as observed at pods H and D. There are anticorrelated fluctuations in T' and q'_v, however, suggesting the passage of a wavelike feature. A similar steady increasing trend in p' is visible at the three additional pods M, L, and N located farther north accompanying bore passage (Figs. 11d–f). Rather, pressure perturbation patterns occurring 10–20 min after bore passage resemble those anticipated: near 0850 UTC at pod K, near 0910 UTC at pod M, near 0910 UTC and 0925 UTC at pod L, near 0905 UTC, 0915 UTC, and 0940 UTC at pod N. Additionally, at the three northernmost surface stations, evidence of wavelike perturbations in T' and q'_v are muted or nonexistent.[6] The UIUC launch point is located near the northern most surface pods (Fig. 1). Surface temperatures are the same in the pre-bore environment depicted by UIUC1 0832 UTC and the post-bore environment depicted by UIUC2 0903 UTC (Figs. 7c,d and 8), consistent with the pod data.

The mountains also impact characteristics of the parent MCS cold pool. The reduction in T' at pods M, L, and N accompanying cold pool passage is half that seen at the three southern stations, consistent with a greater modification to the cold pool by the underlying land surface (i.e., warming) as it moves northward and away from the southern mountain peaks (i.e., the region of successful cold pool mountain crossing). This smaller temperature change may be also due to the cold pool air experiencing larger adiabatic warming as the cold pool descends down the taller mountain peaks.

9. Conclusions

During the early morning hours of 5 November 2018, a MCS propagated discretely as it moved over the second-most populous province of Argentina, Córdoba Province. Its behavior and the associated physical processes responsible for the discrete propagation were influenced by the regional mountains, the Sierras de Córdoba. As the storm approached the windward side of the Sierras de Córdoba from the southwest, isolated convective cells developed in the mountain lee. These cells merged and grew upscale into a new MCS downstream of the mountains as the parent storm decayed. This discrete propagation initiated as the cold pool of the parent MCS moved over the mountains and perturbed the nocturnal stable layer confined in the lee. The cold pool–stable layer interaction generated a leeside bore and trailing gravity waves, which supported the development of cells behind the bore front and the eventual upscale growth into a new MCS (i.e., discrete propagation). Observations and theory suggested the presence of an undular bore within the lower troposphere, specifically an undular bore with mixing supported within a near-surface nocturnal inversion and an undular bore with no mixing supported within an elevated inversion 2500–3000 m AGL.

The bore and trailing gravity waves initiated cell development through two mechanisms. First, their associated convergence provided ascent to initiate the leeside cells along several distinct lines perpendicular to the direction of bore motion. Second, the bore modified the environment in its wake, creating more favorable conditions for convection initiation driven by trailing-gravity wave ascent. The initial bore-driven ascent lifted, cooled, and reduced the magnitude of the two lower-tropospheric inversions, removed the most-unstable parcel CIN, and substantially reduced the surface-based CIN.

[5] Pod K is located 15 km southeast of the city of Alta Gracia (Fig. 1). A line connecting the two points is parallel to the orientation of the wave. Therefore, Alta Gracia and pod K experience the wave passage at a similar time. Based on the RMA1 Z_H, the wave is about to pass over Alta Gracia, and thus pod K, at 0827 UTC (Figs. 9c,d).

[6] At pod L, there may exist instrumentation set up biases in the first 5+ min of data with a 2°C drop in T' and 1 g kg^{-1} drop in q'_v. Based on other existing radar and surface station observations, the time of bore passage is estimated to be 0852 UTC.

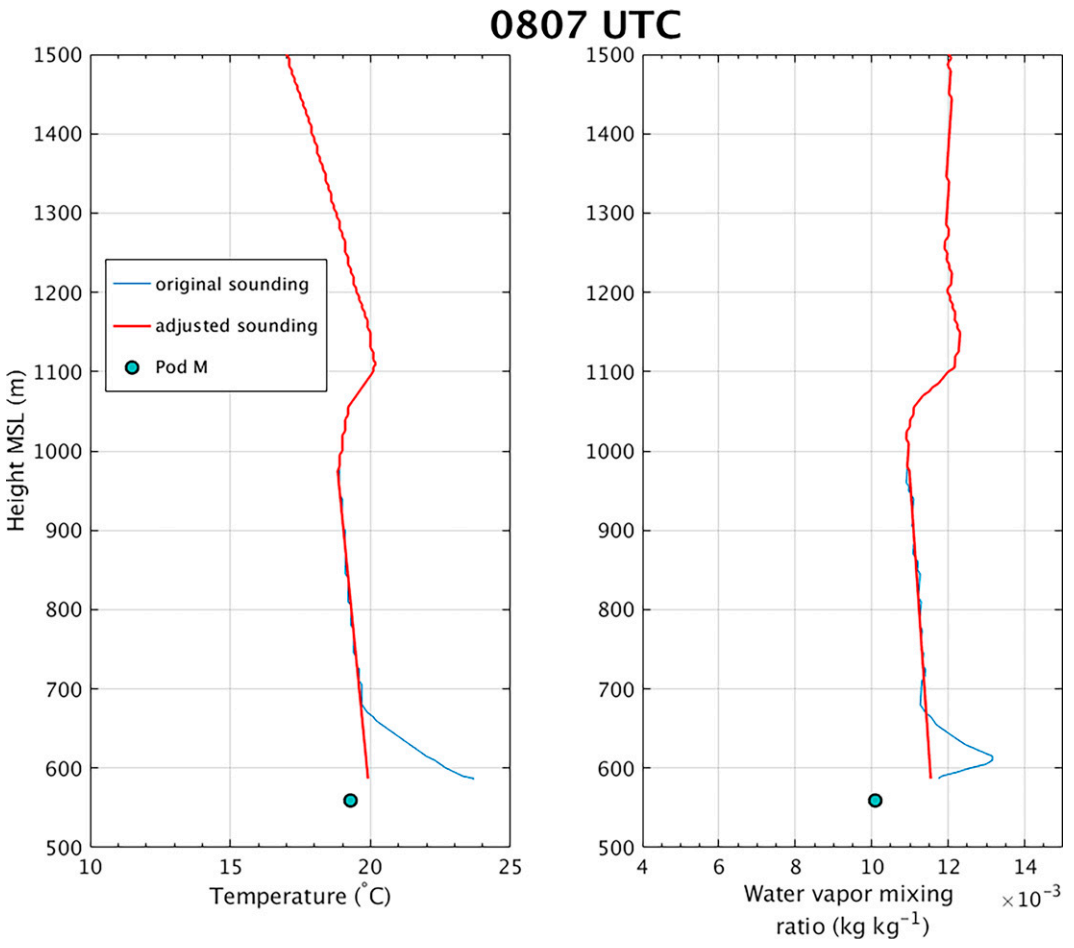

FIG. A1. Lower-tropospheric vertical profiles of (left) temperature, and (right) water vapor mixing ratio, from the original 0807 UTC UIUC sounding (thin blue line), our adjusted sounding (thick red line), and available pod measurement (circle marker).

Bore initiation was likely confined to the lee of the southern portion of the mountain chain. The altitude of the Sierras de Córdoba varies along the north–south chain, with lower peaks along the southern segment of the mountains and taller peaks to the north. The discrete propagation of the MCS only occurred for the portion of the storm that moved over the shorter southern peaks, while the northern portion of the storm stalled over the terrain and eventually decayed. Based on an analysis of the cold pool depth and mountain Froude number, the MCS cold pool was unable to traverse the taller mountain peaks, and therefore unable to perturb the leeside stable layer to generate a bore in this northern region. However, the northeastward propagation of the bore originating from the lee of the southern peaks was able to perturb the environment in the lee of these taller northern mountain peaks, including in regions of minimal CI.

RELAMPAGO–CACTI offered a unique opportunity to study the impact of regional terrain on the discrete propagation of a MCS, while illustrating the necessary spatiotemporal resolution of observations to evaluate the dominant physical processes. Still, a number of questions remain regarding the influence of the Sierras de Córdoba on the movement of the parent MCS cold pool (particularly the role of mountain height variations), mechanisms for bore initiation in the mountain lee, and the support for bores with different characteristics within distinct levels of the atmosphere including the link to surface and radar observations. For example, did the MCS cold pool perturb the elevated stable layer as well as the near-surface stable layer as it moved over the mountain? Were the elevated and near-surface bores a vertically coherent feature with different physical manifestations (i.e., mixing, no mixing) dependent on the ambient conditions within each layer, or were they two independent features? Did the surface stations to the north show little to no bore signal due to a vertical propagation of energy as the bore moved away from its origin or did the nearby mountain play a role? Were the taller peaks of the Sierras Grandes alone detrimental to the discrete propagation of the MCS, or did the presence of the downstream adjacent lower ridge of the Sierras Chicas play a role disrupting the cold pool? Scientific advancements will benefit greatly from additional observations and complementary

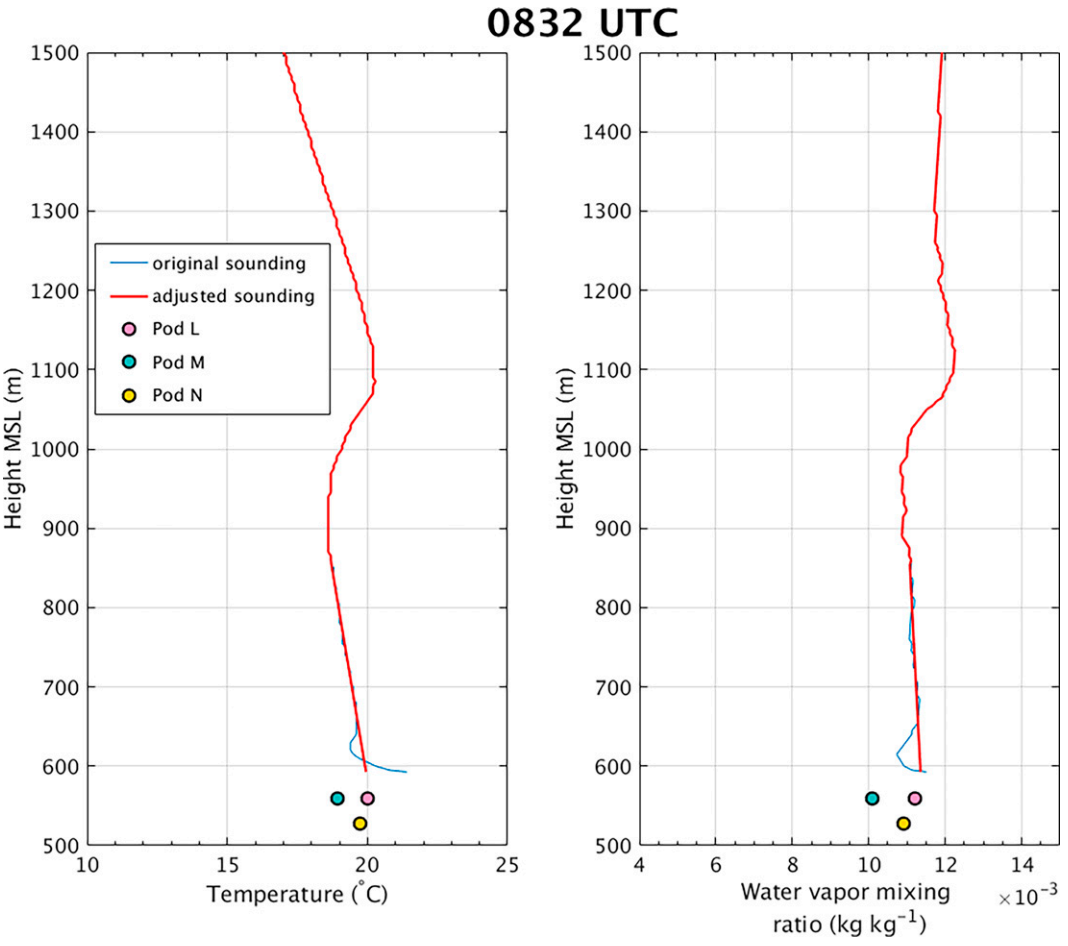

FIG. A2. As in Fig. A1, but for the UIUC 0832 UTC sounding.

process-level numerical experiments, to evaluate the hypotheses posed herein and to discover the likely additional physical processes not yet considered.

Acknowledgments. We greatly thank the National Science Foundation for their generous support for this work through Grant AGS-1661679 (MK), the National Oceanographic and Atmospheric Administration through Grant NA19OAR4590222, and the Office of Naval Research through Grant N000014-17-1-2478 (KL). We also thank Dr. Tony Lyza, Dr. Becky Adams-Selin, and one anonymous reviewer for their comprehensive and insightful comments. Data are provided by NCAR/EOL under the sponsorship of the National Science Foundation.

Data availability statement. All data used during this study are openly available from the National Center for Atmospheric Research/Earth Observing Laboratory under the sponsorship of the National Science Foundation at http://catalog.eol.ucar.edu/relampago. Data from RMA1 in Argentina were provided by Professor Paola Salio at the University of Buenos Aires from the Subsecretaria de Recursos Hídricos, Ministerio del Interior, Obras Publicas y Viviendia, Presidencia de la Nación, Argentina.

APPENDIX

Sounding Adjustment Procedure

Despite the quality control procedures for the soundings posted in the NCAR archive, several of the UIUC soundings exhibited temperature (T) and moisture biases in the lowest 100–200 m that resulted in, for example, unphysical superadiabatic layers. These were removed by the following procedures. First, the unbiased portions of the T and water vapor mixing ratio (q) profiles beneath the low-level inversion were manually identified as layers with constant slope. This slope was determined by linear regression, and the profiles were extrapolated (using the same slope) to the surface, similar to the method used in Gutierrez and Kumjian (2021). Figures A1–A3 show the original profiles in blue, and the adjusted profiles in red for each sounding for which the correction was applied. As a validation, we also plotted

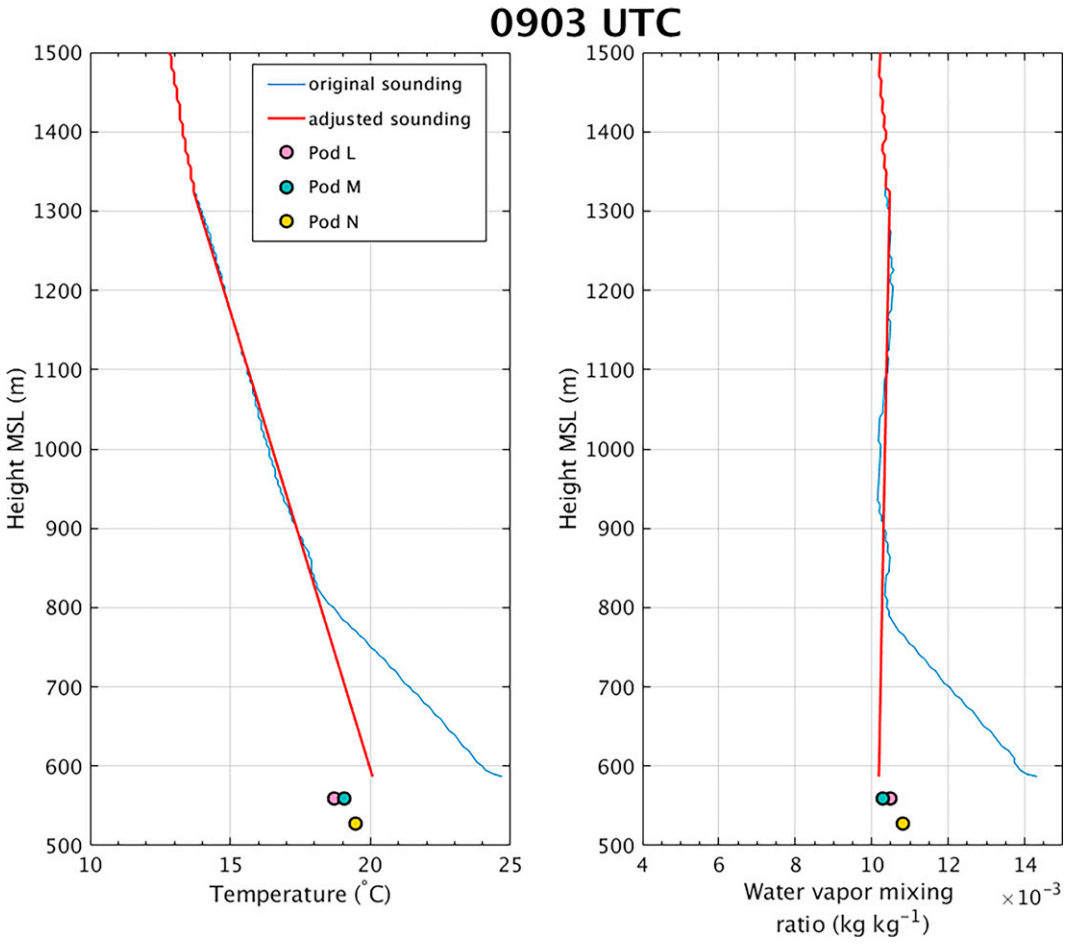

FIG. A3. As in Figs. A1 and A2, but for the UIUC 0903 UTC sounding.

the pod T and q (at the appropriate pressure so as to account for differences in terrain elevation) as circle markers on Figs. A1–A3. Each of the adjusted sounding profiles is within 1°C and 1–2 g kg^{-1} of the pod T and q measurements, respectively.

REFERENCES

Adams-Selin, R. D., 2020: Impact of convectively generated low-frequency gravity waves on evolution of mesoscale convective systems. *J. Atmos. Sci.*, **77**, 3441–3460, https://doi.org/10.1175/JAS-D-19-0250.1.

Alexander, M. J., and J. R. Holton, 2004: On the spectrum of vertically propagating gravity waves generated by a transient heat source. *Atmos. Chem. Phys.*, **4**, 923–932, https://doi.org/10.5194/acp-4-923-2004.

Baines, P. G., 1979: Observations of stratified flow past three-dimensional barriers. *J. Geophys. Res.*, **84**, 7834–7838, https://doi.org/10.1029/JC084iC12p07834.

Banacos, P. C., and M. L. Ekster, 2010: The association of the elevated mixed layer with significant severe weather events in the northeastern United States. *Wea. Forecasting*, **25**, 1082–1102, https://doi.org/10.1175/2010WAF2222363.1.

Browning, K. A., and R. Wexler, 1968: The determination of kinematic properties of a wind field using Doppler radar. *J. Appl. Meteor.*, **7**, 105–113, https://doi.org/10.1175/1520-0450(1968)007<0105:TDOKPO>2.0.CO;2.

Bryan, G. H., and M. D. Parker, 2010: Observations of a squall line and its near environment using high-frequency rawinsonde launches during VORTEX2. *Mon. Wea. Rev.*, **138**, 4076–4097, https://doi.org/10.1175/2010MWR3359.1.

Charba, J., 1974: Application of gravity current model to analysis of squall line gust front. *Mon. Wea. Rev.*, **102**, 140–156, https://doi.org/10.1175/1520-0493(1974)102<0140:AOGCMT>2.0.CO;2.

Christie, D. R., 1989: Long nonlinear waves in the lower atmosphere. *J. Atmos. Sci.*, **46**, 1462–1491, https://doi.org/10.1175/1520-0469(1989)046<1462:LNWITL>2.0.CO;2.

——, K. J. Muirhead, and A. L. Hales, 1978: On solitary waves in the atmosphere. *J. Atmos. Sci.*, **35**, 805–825, https://doi.org/10.1175/1520-0469(1978)035<0805:OSWITA>2.0.CO;2.

Chu, C., and Y. Lin, 2000: Effects of orography on the generation and propagation of mesoscale convective systems in a two-dimensional conditionally unstable flow. *J. Atmos. Sci.*, **57**, 3817–3837, https://doi.org/10.1175/1520-0469(2001)057<3817:EOOOTG>2.0.CO;2.

Coleman, T. A., K. R. Knupp, and D. E. Herzmann, 2010: An undular bore and gravity waves illustrated by dramatic time-

lapse photography. *J. Atmos. Oceanic Technol.*, **27**, 1355–1361, https://doi.org/10.1175/2010JTECHA1472.1.

Crook, N. A., 1988: Trapping of low-level internal gravity waves. *J. Atmos. Sci.*, **45**, 1533–1541, https://doi.org/10.1175/1520-0469(1988)045<1533:TOLLIG>2.0.CO;2.

——, and M. W. Moncrieff, 1988: The effect of large-scale convergence on the generation and maintenance of deep moist convection. *J. Atmos. Sci.*, **45**, 3606–3624, https://doi.org/10.1175/1520-0469(1988)045<3606:TEOLSC>2.0.CO;2.

Doviak, R. J., and R. Ge, 1984: An atmospheric solitary gust observed with a Doppler radar, a tall tower and a surface network. *J. Atmos. Sci.*, **41**, 2559–2573, https://doi.org/10.1175/1520-0469(1984)041<2559:AASGOW>2.0.CO;2.

——, and D. S. Zrnić, 1993: *Doppler Radar and Weather Observations.* 2nd ed. Dover Publications, Inc., 562 pp.

Engerer, N. A., and D. J. Stensrud, 2008: Surface characteristics of observed cold pools. *Mon. Wea. Rev.*, **136**, 4839–4849, https://doi.org/10.1175/2008MWR2528.1.

Fortune, M., 1980: Properties of African squall lines inferred from time-lapse satellite imagery. *Mon. Wea. Rev.*, **108**, 153–168, https://doi.org/10.1175/1520-0493(1980)108<0153:POASLI>2.0.CO;2.

Fovell, R. G., 2002: Upstream influence of numerically simulated squall-line storms. *Quart. J. Roy. Meteor. Soc.*, **128**, 893–912, https://doi.org/10.1256/0035900021643737.

——, G. L. Mullendore, and S.-H. Kim, 2006: Discrete propagation of numerically simulated nocturnal squall lines. *Mon. Wea. Rev.*, **134**, 3735–3752, https://doi.org/10.1175/MWR3268.1.

Frame, J., and P. Markowski, 2006: The interaction of simulated squall lines with idealized mountain ridges. *Mon. Wea. Rev.*, **134**, 1919–1941, https://doi.org/10.1175/MWR3157.1.

Fujita, T. T., 1963: Analytical mesometeorology: A review. *Severe Local Storms, Meteor. Monogr.* No. 5, Amer. Meteor. Soc., 77–125.

Fulton, J., D. S. Zrnić, and R. J. Doviak, 1990: Initiation of a solitary wave family in the demise of a nocturnal thunderstorm density current. *J. Atmos. Sci.*, **47**, 319–337, https://doi.org/10.1175/1520-0469(1990)047<0319:IOASWF>2.0.CO;2.

Geerts, B., and Coauthors, 2017: The 2015 Plains Elevated Convection At Night field project. *Bull. Amer. Meteor. Soc.*, **98**, 767–786, https://doi.org/10.1175/BAMS-D-15-00257.1.

Goff, R. C., 1976: Vertical structure of thunderstorm outflows. *Mon. Wea. Rev.*, **104**, 1429–1440, https://doi.org/10.1175/1520-0493(1976)104<1429:VSOTO>2.0.CO;2.

Grasmick, C., B. Geerts, D. D. Turner, Z. Wang, and T. M. Weckwerth, 2018: The relation between nocturnal MCS evolution and its outflow boundaries in the stable boundary layer: An observational study of the 15 July 2015 MCS in PECAN. *Mon. Wea. Rev.*, **146**, 3203–3226, https://doi.org/10.1175/MWR-D-18-0169.1.

Groff, F. P., R. D. Adams-Selin, and R. S. Schumacher, 2021: Response of MCS low-frequency gravity waves to vertical wind shear and nocturnal thermodynamic environments. *J. Atmos. Sci.*, **104**, 3889–3908, https://doi.org/10.1175/JAS-D-20-0208.1.

Gutierrez, R. E., and M. R. Kumjian, 2021: Environmental and radar characteristics of gargantuan hail-producing storms. *Mon. Wea. Rev.*, **149**, 2523–2538, https://doi.org/10.1175/MWR-D-20-0298.1.

Haghi, K. R., and D. R. Durran, 2021: On the dynamics of atmospheric bores. *J. Atmos. Sci.*, **78**, 313–327, https://doi.org/10.1175/JAS-D-20-0181.1.

——, D. B. Parsons, and A. Shapiro, 2017: Bores observed during IHOP_2002: The relationship of bores to the nocturnal environment. *Mon. Wea. Rev.*, **145**, 3929–3946, https://doi.org/10.1175/MWR-D-16-0415.1.

——, and Coauthors, 2019: Bore-ing into nocturnal convection. *Bull. Amer. Meteor. Soc.*, **100**, 1103–1121, https://doi.org/10.1175/BAMS-D-17-0250.1.

Houze, R. A., 1977: Structure and dynamics of a tropical squall-line system. *Mon. Wea. Rev.*, **105**, 1540–1567, https://doi.org/10.1175/1520-0493(1977)105<1540:SADOAT>2.0.CO;2.

——, 2004: Mesoscale convective systems. *Rev. Geophys.*, **42**, RG4003, https://doi.org/10.1029/2004RG000150.

Johnson, A., X. Wang, K. R. Haghi, and D. B. Parsons, 2018: Evaluation of forecasts of a convectively generated bore using an intensively observed case study from PECAN. *Mon. Wea. Rev.*, **146**, 3097–3122, https://doi.org/10.1175/MWR-D-18-0059.1.

Knupp, K. R., 2006: Observational analysis of a gust from to bore to solitary wave transition within an evolving nocturnal boundary layer. *J. Atmos. Sci.*, **63**, 2016–2035, https://doi.org/10.1175/JAS3731.1.

Koch, S. E., and W. L. Clark, 1999: Structure of an internal bore and dissipating gravity current as revealed by Raman lidar. *Mon. Wea. Rev.*, **119**, 857–887, https://doi.org/10.1175/1520-0493(1991)119<0857:SOAIBA>2.0.CO;2.

——, P. B. Dorian, R. Ferrare, S. H. Melfi, W. C. Skillman, and D. Whiteman, 1991: Structure of an internal bore and dissipating gravity current as revealed by Raman lidar. *Mon. Wea. Rev.*, **119**, 857–887, https://doi.org/10.1175/1520-0493(1991)119<0857:SOAIBA>2.0.CO;2.

——, W. Feltz, F. Fabry, M. Pagowski, B. Geerts, K. M. Bedka, D. O. Miller, and J. W. Wilson, 2008a: Turbulent mixing processes in atmospheric bores and solitary waves deduced from profiling systems and numerical simulation. *Mon. Wea. Rev.*, **136**, 1373–1400, https://doi.org/10.1175/2007MWR2252.1.

——, C. Flamant, J. W. Wilson, B. M. Gentry, and B. D. Jamison, 2008b: An atmospheric soliton observed with Doppler radar, differential absorption lidar, and a molecular Doppler lidar. *J. Atmos. Oceanic Technol.*, **25**, 1267–1287, https://doi.org/10.1175/2007JTECHA951.1.

Kotthaus, S., E. O'Connor, C. Münkel, C. Charlton-Perez, M. Haeffelin, A. M. Gabey, and C. S. B. Grimmons, 2016: Recommendations for processing atmospheric attenuated backscatter profiles from Vaisala CL31 ceilometers. *Atmos. Meas. Tech.*, **9**, 3769–3791, https://doi.org/10.5194/amt-9-3769-2016.

Kumjian, M. R., and K. A. Lombardo, 2017: Insights into the evolving microphysical and kinematic structure of northeastern U.S. winter storms from dual-polarization Doppler radar. *Mon. Wea. Rev.*, **145**, 1033–1061, https://doi.org/10.1175/MWR-D-15-0451.1.

Lane, T. P., and M. J. Reeder, 2001: Convectively generated gravity waves and their effect on the cloud environment. *J. Atmos. Sci.*, **58**, 2427–2440, https://doi.org/10.1175/1520-0469(2001)058<2427:CGGWAT>2.0.CO;2.

Lindzen, R. S., and K.-K. Tung, 1976: Banded convective activity and ducted gravity waves. *Mon. Wea. Rev.*, **104**, 1602–1617, https://doi.org/10.1175/1520-0493(1976)104<1602:BCAADG>2.0.CO;2.

Lombardo, K., 2020: Squall lines response to coastal mid-Atlantic thermodynamic heterogeneities. *J. Atmos. Sci.*, **77**, 4143–4170, https://doi.org/10.1175/JAS-D-20-0044.1.

——, and T. Kading, 2018: The behavior of squall lines in horizontally heterogeneous coastal environments. *J. Atmos. Sci.*, **75**, 1243–1269, https://doi.org/10.1175/JAS-D-17-0248.1.

Long, R. R., 1972: Finite amplitude disturbances in the flow of inviscid rotating and stratified fluids over obstacles. *Annu. Rev.*

Fluid Mech., **4**, 69–92, https://doi.org/10.1146/annurev.fl.04.010172.000441.

Loveless, D. M., T. J. Wagner, D. D. Turner, S. A. Ackerman, and W. F. Feltz, 2019: A composite perspective on bore passages during the PECAN campaign. *Mon. Wea. Rev.*, **147**, 1395–1413, https://doi.org/10.1175/MWR-D-18-0291.1.

Mapes, B. E., 1993: Gregarious tropical convection. *J. Atmos. Sci.*, **50**, 2026–2037, https://doi.org/10.1175/1520-0469(1993)050<2026:GTC>2.0.CO;2.

Nesbitt, S. W., and Coauthors, 2021: A storm safari in subtropical South America: Proyecto RELAMPAGO. *Bull. Amer. Meteor. Soc.*, **102**, E1621–E1644, https://doi.org/10.1175/BAMS-D-20-0029.1.

Newton, C. W., and J. C. Fankhauser, 1975: Movement and propagation of multicellular convective storms. *Pure Appl. Geophys.*, **113**, 747–764, https://doi.org/10.1007/BF01592957.

Nicholls, M. E., R. A. Pielke, and W. R. Cotton, 1991: Thermally forced gravity waves in an atmosphere at rest. *J. Atmos. Sci.*, **48**, 1869–1884, https://doi.org/10.1175/1520-0469(1991)048<1869:TFGWIA>2.0.CO;2.

Parsons, D. B., K. R. Haghi, K. T. Halbert, and B. Elmer, 2019: The potential role of atmospheric bores and gravity waves in the initiation and maintenance of nocturnal convection over the southern Great Plains. *J. Atmos. Sci.*, **76**, 43–68, https://doi.org/10.1175/JAS-D-17-0172.1.

Pierrehumbert, R. T., and B. Wyman, 1985: Upstream effects of mesoscale mountains. *J. Atmos. Sci.*, **42**, 977–1003, https://doi.org/10.1175/1520-0469(1985)042<0977:UEOMM>2.0.CO;2.

Reeves, H. D., and Y. Lin, 2007: The effects of a mountain on the propagation of a preexisting convective system for blocked and unblocked flow regimes. *J. Atmos. Sci.*, **64**, 2401–2421, https://doi.org/10.1175/JAS3959.1.

Rosenthal, S. L., 1980: Numerical simulation of tropical cyclone development with latent heat release by the resolvable scales. II: Propagating small-scale features observed in the prehurricane phase. NOAA Tech. Rep. ERL 413-AOML 29, 43 pp.

Rottman, J. W., and J. E. Simpson, 1989: The formation of internal bores in the atmosphere: A laboratory model. *Quart. J. Roy. Meteor. Soc.*, **115**, 941–963, https://doi.org/10.1002/qj.49711548809.

Scorer, R. S., 1949: Theory of waves in the lee of mountains. *Quart. J. Roy. Meteor. Soc.*, **75**, 41–56, https://doi.org/10.1002/qj.49707532308.

Servicio Meteorólogico Nacional, Argentina, 2019: SMN radiosonde data, version 1.0. UCAR/NCAR–Earth Observing Laboratory, accessed 1 April 2020, https://doi.org/10.26023/E8MP-0GD3-4903.

Smith, R. B., 1979: The influence of mountains on the atmosphere. *Advances in Geophysics*, Vol. 21, Academic Press, 87–230, https://doi.org/10.1016/S0065-2687(08)60262-9.

Su, T., and G. Zhai, 2017: The role of convectively generated gravity waves on convective initiation: A case study. *Mon. Wea. Rev.*, **145**, 335–359, https://doi.org/10.1175/MWR-D-16-0196.1.

Tepper, M., 1950: A proposed mechanism of squall lines: The pressure jump line. *J. Meteor.*, **7**, 21–29, https://doi.org/10.1175/1520-0469(1950)007<0021:APMOSL>2.0.CO;2.

UCAR/NCAR Earth Observing Laboratory, 2020: Multi-network composite highest resolution radiosonde data version 1.3. UCAR/NCAR–Earth Observing Laboratory, accessed 22 June 2020, https://doi.org/10.26023/GKFF-YNBJ-BV14.

Varble, A. C., and Coauthors, 2021: Utilizing a storm-generating hotspot to study convective cloud transitions: The CACTI Experiment. *Bull. Amer. Meteor. Soc.*, **102**, E1597–E1620, https://doi.org/10.1175/BAMS-D-20-0030.1.

Vescio, M. D., and R. H. Johnson, 1992: The surface-wind response to transient mesoscale pressure fields associated with squall lines. *Mon. Wea. Rev.*, **120**, 1837–1850, https://doi.org/10.1175/1520-0493(1992)120<1837:TSWRTT>2.0.CO;2.

Wakimoto, R. M., 1982: The life cycle of thunderstorm gust fronts as viewed with Doppler radar and rawinsonde data. *Mon. Wea. Rev.*, **110**, 1060–1082, https://doi.org/10.1175/1520-0493(1982)110<1060:TLCOTG>2.0.CO;2.

Weckwerth, T. M., and Coauthors, 2004: An overview of the International H_20 Project (IHOP_2002) and some preliminary highlights. *Bull. Amer. Meteor. Soc.*, **85**, 253–278, https://doi.org/10.1175/BAMS-85-2-253.

——, K. J. Weber, D. D. Turner, and S. M. Spuler, 2016: Validation of a water vapor micropulse differential absorption lidar (dial). *J. Atmos. Sci.*, **33**, 2353–2372, https://doi.org/10.1175/JTECH-D-16-0119.1.

——, J. Hanesiak, J. W. Wilson, S. B. Trier, S. K. Degelia, W. A. Gallus, R. D. Roberts, and X. Wang, 2019: Nocturnal convection initiation during PECAN 2015. *Bull. Amer. Meteor. Soc.*, **100**, 2223–2239, https://doi.org/10.1175/BAMS-D-18-0299.1.

Wilson, J. W., and W. E. Schreiber, 1986: Initiation of convective storms at radar-observed boundary-layer convergence lines. *Mon. Wea. Rev.*, **114**, 2516–2536, https://doi.org/10.1175/1520-0493(1986)114<2516:IOCSAR>2.0.CO;2.

Wood, I. R., and J. E. Simpson, 1984: Jumps in layered miscible fluids. *J. Fluid Mech.*, **140**, 329–342, https://doi.org/10.1017/S0022112084000628.

Wurman, J., D. Dowell, Y. P. Richardson, P. M. Markowski, E. N. Rasmussen, D. W. Burgess, L. J. Wicker, and H. B. Bluestein, 2012: The Second Verification of the Origins of Rotation in Tornadoes Experiment: VORTEX2. *Bull. Amer. Meteor. Soc.*, **93**, 1147–1170, https://doi.org/10.1175/BAMS-D-11-00010.1.

Zhang, J., D. B. Parsons, and Y. Wang, 2020: Wave disturbances and their role in the maintenance, structure, and evolution of a mesoscale convective system. *J. Atmos. Sci.*, **77**, 51–77, https://doi.org/10.1175/JAS-D-18-0348.1.